

3D inkjet printing of biomaterials with strength reliability and cytocompatibility: Quantitative process strategy for Ti-6Al-4V

Srimanta Barui^{a,d}, Asish K. Panda^{a,d}, S. Naskar^{a,c}, Kuppuraj R.^b, Saptarshi Basu^b and

Bikramjit Basu^{a,c,d*}

^aLaboratory for Biomaterials, Materials Research Centre, Indian Institute of Science, Bangalore, India

^bCombustion and Laser Diagnostics Lab, Department of Mechanical Engineering, Indian Institute of Science, Bangalore, India

^cCentre for Biosystems Science and Engineering, Indian Institute of Science, Bangalore, India

^dCentre of Excellence and Innovation in Biotechnology – ‘Translational Center on Biomaterials for Orthopaedic and Dental Applications, Materials Research Center, IISc Bangalore, India

Abstract

Among additive manufacturing (AM) techniques, laser or electron beam based processes have been widely investigated for metallic implants. Despite the potential in manufacturing of patient-specific biomedical implants, 3D inkjet powder printing (3DIJPP, a variant of AM) of biomaterials is still in its infancy, as little is known quantitatively about the transient process physics and dynamics. An equally important challenge has been the ink formulation to manufacture biomaterials with reliable mechanical properties and desired biocompatibility. We have developed, for the very first time, the theoretical foundation and experimental formulation of a unique process strategy involving the ‘on-demand’ delivery of a novel *in situ* polymerisable acrylic ink system to print a model biomaterial, Ti-6Al-4V. The post-ejection in-flight dynamics of ink droplets have been captured *in situ* by employing high speed stroboscopic shadowgraphy, to quantitatively estimate the dimensionless numbers of fluid physics for ‘printability’ assessment. Washburn model was adapted extensively to quantify the capillary ink infiltration time in porous powder bed of finite thickness. On the other hand, particle tracking mode in diffusing wave spectroscopy (DWS) was exploited to analyse the timescale for effective binding of powder particles during *in situ* polymerisation. The clinically relevant combination of 3D porous architecture with 98.4% interconnectivity among 10–40 μm pores together with modest combination of elastic modulus (4 GPa) and strength reliability (Weibull modulus ~ 8.1) establish the potential of inkjet printed Ti-6Al-4V as cortical bone analogue. A better cell attachment, viability, cytoskeletal spreading with pronounced proliferation of murine fibroblasts and pre-osteoblasts on 3DIJPP Ti-6Al-4V, when benchmarked against the metallurgically processed (commercial) or selective laser melted (SLM) Ti-6Al-4V, has been demonstrated, *in vitro*. The enhanced cellular activities on the 3DIJPP Ti-6Al-4V was explained in terms of an interplay among the elastic stiffness, surface roughness and wettability against the same benchmarking. It is conceived that the quantitative understanding of the integrated process physics and dynamics to print Ti-6Al-4V with reliable mechanical properties together with better cytocompatibility can lead to a paradigm shift in adapting the scalable 3DIJPP for manufacturing of metallic biomaterials.

Keywords: Titanium; 3D inkjet printing; capillary infiltration-Washburn model; micro-computed tomography; Weibull statistics; cytocompatibility; **Corresponding author:** E-mail: bikram@iisc.ac.in

1. Introduction

In the field of biomedical engineering, additive manufacturing (AM) is expected to revolutionise the manufacturing of patient-specific implant and tissue engineered scaffolds as personalized regenerative medicine for treatment of human diseases[1-10]. Though the generic term, AM encompasses a wide spectrum of manufacturing techniques, computer aided design (CAD) driven layer-by-layer addition of materials has been used as a processing concept in all such variants. In particular, the commercially available AM facilities can be classified in three broad divisions. First, the laser-based technology is based on sintering/melting metal powders layer-by-layer or curing liquid monomer/polymer, according to machine readable CAD data. The second one addresses the on-demand jetting/printing of binder droplets on powdered material, while the third category involves the use of controlled deposition of pasty materials through micro-nozzles. A comparison among different AM techniques along with their pros and cons are described elsewhere [11]. The last two fabrication approaches can be pursued at ambient temperature, implicating the applicability in patterning biological cells and/or plotting cell laden biomaterials[12-14]. Inkjet 3D powder printing (3DIJPP), a variant of AM technologies, was invented at Massachusetts Institute of Technology, USA in the year 1993. This is also popularly known as “powder bed and inkjet head” or “binderjet printing”. While laser or electron-beam based AM techniques are widely being investigated to manufacture metallic implants, it is expected that 3DIJPP, currently used for producing steel based engineering components, can be adapted in near future for biomedical implant manufacturing, as paved in this work.

The functioning of thermal inkjet printing relies on the principle of on-demand delivery of pre-determined amount of ink (drop-on-demand), synchronised with the deposition of powders in layer-by-layer manner, based on the specific design of the scaffold. A number of

researches still use ‘black box’ approach in adapting 3DIJPP to fabricate a variety of materials. Based on various multidisciplinary approaches involving stroboscopic shadowgraphy and relevant elements of fluid physics, the physics and dynamics of the transient processes involved in 3D inkjet printing are revealed. In particular, the conceptual elements of fluid dynamics and fluid physics are effectively utilised to understand the pre-impact ink droplet flight and post-impact ink-powder interaction. It is perceived that the quantitative understanding of the fluid physics of in-flight ink droplets and post-impact interaction with the powder bed, can pave the accelerated adaptability to manufacture biomaterials.

In this paper, we report the formulation of a novel *in-situ* polymerisable acrylic based ink system, capable to print Ti-6Al-4V (FDA approved biomaterial), starting from biomedical grade powders. It will be shown how the strategic modification of powders can be adapted together with printable ink system to manufacture 3D porous metallic architectures. The clinical application potential was explored in the prototype development of human femoral stem for total hip replacement and cranioplasty, to rehabilitate human skull bone flap in the post-operative stage of decompressive craniectomy.

A range of multiresolution microstructural and mechanical characterisation was subsequently utilised to understand the impact of the adopted processing strategy on microstructure-property correlation for lab-scale coupon samples of Ti6Al4V. The phase assemblage and 3D microstructures (micro-computed tomography) of as-printed and sintered architectures were investigated. Two-parameter Weibull statistics was employed to evaluate the strength reliability of 3D inkjet printed Ti-6Al-4V. More importantly, the cell-material interaction of 3D inkjet printed Ti-6Al-4V was probed using mammalian fibroblasts and primary osteoblasts, with a particular emphasis to understand the cell viability, proliferation and cytoskeletal spreading, *in vitro*.

2. Materials and Methods

2.1 Ink preparation, ink physical properties and metal powder modification strategy:

An aqueous solution of 22% (wt/vol) acrylamide (SDFCL, Mumbai, India) was prepared as the base ink with the addition of 1.0 – 2.0% (vol/vol) N,N,N',N'-tetramethylethane-1,2-diamine (TEMED, Spectrochem, Mumbai, India). This precursor solution was stirred for 15 minutes with a magnetic stirrer until it appears to be a clear solution, followed by filtration through Whatman 40 filter paper. Biomedical grade Ti-6Al-4V (NANOSHEL, Delaware, USA) as the model biomaterial having particle size 10 – 20 μm , were modified with 2 – 8% (wt/wt) (preferably 4 wt.%) ammonium persulfate (APS, SDFCL, Mumbai, India) in dry ball mill using tungsten carbide (WC) balls and vial for 30 minutes. In addition, calcium sulfate hemihydrate (Plaster of Paris, POP) was also modified using similar method (data not shown) for patient specific cranium vault fabrication. As APS is highly hygroscopic and the reactivity (free radical generation) decreases with moisture absorption, the modified powder should be preserved in desiccated container. All chemicals used were of analytical grade (AR).

The static and dynamic viscosities of the ink were measured using a cone-plate viscometer (DHR3, TA instruments, USA) using flow sweep and frequency sweep respectively. The shear rate was varied from 0.1 s^{-1} to 100 s^{-1} , having 5 data-points per decade, with duration of 5 minutes. The frequency sweep was carried out using oscillation frequency ranging from 0.1 rad/s to 100 rad/s, with a constant strain of 0.1%. A contact angle goniometer (OCA 15EC, Dataphysics®, Germany) was utilised in pendant drop mode, to measure the surface tension of the ink. The pH of the ink was measured in a digital pH meter (CyberScan pH Tutor, Eutech Instruments, Singapore). All of the experiments described above were carried out at room temperature (25°C).

2.2 High speed *in-situ* imaging of ink droplets

The kinematic information (velocity and diameter) of the droplets, ejected from inkjet nozzle head, were acquired using high-speed shadowgraphy equipments. The plane of the droplets, dispensed from the nozzle head were back illuminated with a high-intensity strobe lamp. Subsequently, the shadow images of the droplets were acquired by a high speed camera placed along the optical path. The camera shutter speed was synchronised with strobe lamp pulse rate to yield time frozen snapshot of the travelling droplets. Since the order of droplet size was very small (40-50 μm) in the spray, telescopic microscope was coupled to the camera to focus at a small region of interest in the spray. In this study, 2X magnification lens was utilised to cover a square region of 1.9 mm in the spatial domain.

All the images were acquired at 60,000 fps with an acquisition time of ~ 0.14 s (i.e. 8454 images in each step). The acquired images were reconstructed and post-processed in Lavisision Particle master™ (Göttingen, Germany) shadow module to quantify the droplet size and velocity. The algorithm involved two step thresholding segmentation method to calculate the droplet size (D) and velocity (v). From the obtained results, the parameters, like D_{\min} , D_{\max} , D_{ave} , v_{\min} and v_{\max} were quantified.

2.3 Helium gas pycnometry of powder bed: volume porosity of as deposited powder

He-gas pycnometry is a reliable technique to determine true material volume and true density. Helium gas is the lightest gas after hydrogen, capable to infiltrate through any possible physical pore, giving rise to the process to be very accurate. Based on Archimedes principle, this methodology assures to handle powder based material, which is not possible in liquid porosimetry (e.g. water or mercury porosimetry). The machine (ULTRAPYC 1200e, Quantachrome, USA) was calibrated using an automatic iterative process until a standard

deviation of <0.005 was attained. 5 rectangular polymeric vessels were 3D printed using a UV curing based polyjet 3D printer (Stratasys™) having the dimensions of $6\text{mm}\times 7.3\text{mm}\times 10\text{mm}$ and 1 mm wall thickness. The empty vessels were loaded in the pycnometer chamber to measure their total volume. Next, the modified Ti-6Al-4V powder was poured in 3D printed vessels with gentle tapping to mimic the powder bed deposited during the inkjet powder printing. Similarly, the powder-loaded vessels were put in the pycnometer chamber to record the cumulative volume of vessels and the powder. The volume of the powder is subtracted and normalized with the internal cavity volume of the individual vessel. He-gas pycnometry based measurements provides us the information of the material volume fraction and the pore volume fraction.

2.4 Washburn capillary rise (WCR): dynamic contact angle of ink with porous bed

Washburn capillary rise method is useful to investigate the wettability of porous bed by the liquid ink. According to the methodology reported elsewhere[15, 16], two liquids were allowed to infiltrate through a reproducible powder bed independently, while one of them was a reference, completely wetting liquid (contact angle = 0°) and the other to be the aqueous ink. For this experiment, two identical cylindrical aluminium cells were prepared (length 72 mm, ID 16 mm and thickness 1.5 mm) with a perforated bottom surface having 60 holes in each cell. To prevent leakage of powder during the capillary rise, a thin filter paper disk was placed at the bottom of the cells before loading the powder. After gently tapping the powder (e.g. Ti-6Al-4V), the cells were capped with cotton and centrifuged at 3000 rpm for 10 minutes. This technique is popular for its ability to provide reproducible packing of powder bed. Hexane was used as reference liquid and the packed cylinder was hung from a wire frame attached to the balance. This arrangement facilitates the perforated surface of the cell to immerse sufficiently into the liquid[17]. The identical procedure was repeated for the ink as well. As

soon as the perforated surface touched the liquid meniscus, the weight initially decreased due to buoyancy, followed by subsequent increase due to liquid penetration into the powder bed column. The squared values of the gained weight (due to capillary infiltration) versus time were plotted for both the ink and hexane. Subsequently, the slopes were calculated to find out the contact angle. Ti-6Al-4V powder was used as a model material and the experiment was repeated at least three times each for the ink and the reference liquid to achieve reproducibility.

2.5 Microrheology assessment for polymerisable ink (Diffusing wave spectroscopy)

Dynamic micro-rheology of the *in situ* polymerisation was investigated using a diffusing wave spectroscope (Rheolab II, LS Instruments, Switzerland), equipped with multispeckle echo detector. DWS is a passive and non-intrusive micro-rheological technique, where the incident laser experiences multiple scattering due to turbidity of tracer micro-particles in the sample media (in this case, the polymerising media) providing the information of their transient dynamics in micron length scales[18]. Mean square displacement (MSD) $\langle \Delta r^2(t) \rangle$ of the tracer particles can be measured using the intensity autocorrelation function (ICF, g_2),

$$g_2(t) = 1 + \exp \left[-\frac{1}{6} q^2 \langle \Delta r^2(t) \rangle \right] \dots\dots\dots (1)$$

where q is the scattering vector which is related to the scattering angle (θ) by $q = 4\pi / \lambda_{dws} \sin \theta$. The diffusion coefficient of tracer particle can be further determined from MSD[19],

$$\langle \Delta r^2(t) \rangle = 6Dt \dots\dots\dots (2)$$

where, D is diffusion coefficient and t is the lag time. The nature of the turbid particle dynamics was correlated with the half-life of ICF decay[20, 21]. The half decay time was obtained from the mid-point of the onset and offset of a decay curve.

Against the above, the dynamic microrheological properties of the ink system were quantitatively analysed. As a first step, the aqueous acrylamide solution (22% wt/vol), added with accelerator (1.0 – 2.0% vol/vol TEMED) and tracer particles (5% wt/vol. polystyrene beads, 800 nm, Sigma Aldrich) were taken in a glass cuvette with 10 mm optical path length. In order to probe the dynamics of polystyrene beads during the *in situ* polymerisation, pre-determined quantity of persulfate initiator (see **section 3.4** and **4.1**) was added to the system at the onset of the experiment and the transmitted fluctuation of the incident laser radiation (wavelength 678 nm) was being detected. During the polymerisation session, the data were collected intermittently at 40s intervals up to ~360s. The experiment was carried out at 40°C to maintain consistency with the ambience of inkjet powder printing. The minimum time required to achieve considerable steadiness in diffusion coefficient of the tracer particles in the polymerising media was investigated for various concentrations of APS.

2.6 3D powder printing of Ti-6Al-4V

Solid geometries of cylinder (10 mm×15 mm, $d \times h$), disk (25 mm×10 mm, $d \times h$), rectangular parallelepipeds (7mm×7mm×30mm, $b \times d \times l$) and a human femoral stem prototype were designed in Solidworks™ (Dassault Systèmes, USA). As per the approved clinical trial protocol, patient CT scan data of a patient's cranium (M 37Y) with defective skull vault was obtained from Ramaiah Memorial Hospital, Bangalore (India). The as-received DICOM data was segmented for the skull bone followed by reconstruction using 3D Slicer (open source) software and exported in *.stl (standard tessellation language) format. The feed bed of the printer (Spectrum Z510, formerly Z Corp, USA) was loaded with the persulfate modified powder and the printhead (HP™ no. 11) was purged with the acrylic ink (see **Fig. 1a-c**). The supply line was primed accordingly to establish air free continuity between the printhead and the storage tank. It is quite obvious for printing of multi-materials, depending on the

morphology and size distribution of the powder, the resolution and 3D microstructure depend on various machine settings and optimizing them for each case is essential[4].

In the present study, the print resolution and layer thickness were 600×540 dpi (42µm × 46 µm) and 100 µm, respectively. The ink/binder saturation and build temperature were maintained at 100 – 150% and ~40°C (close to physiological temperature, 37°C), while the deposition speed was 7 layers/min throughout the printing process. Followed by the fabrication of coupon samples (at least 10 samples each for cylinders (for compression test) and disks (for Vickers hardness test) and 18 bar specimens for Weibull modulus analysis on flexural strength) and the cranioplasty model, the designed human femoral stem was also printed using Ti-6Al-4V with excellent dimensional precision and as-printed strength (see **Fig. 1f-j**). After completion of the printing, the as-printed structures were depowdered with the help of compressed air. Next, the 3D objects were retrieved and incubated in a hot air oven at 50 – 60°C for two hours to facilitate completion of the polymerisation and subsequent drying. After this, the stone-hard green bodies were kept in a vacuum desiccator for overnight.

The plaster-of-Paris (POP) based defective skull vault was filled with doughy clay to achieve the symmetry both locally and globally with the other half with respect to the mid-sagittal plane. Once the clay was dried, low viscous paste of bone cement (PMMA) was subsequently casted onto it to obtain the prosthesis having the exact thickness and topography of the missing bone, both internally and externally. The cast was left overnight for complete cure prior to sterilisation (standard protocol prior to real implantation, the current one is proof-of-concept). The above described femoral stem prototype (non-functional) and cranioplast was manufactured to demonstrate wider applicability of the 3DIJPP approach and those prototypes were not tested so far.

The dried Ti-6Al-4V femoral stem and the coupon samples were heat treated in argon atmosphere at 1400°C for 2 hours. The first ramp was continued up to 450°C at the rate of 5°C/min, followed by the second ramp at the rate of 10°C/min up to 1400°C. The alumina tube along with the specimens was purged off with high flow of argon (flow rate ~2.0 l/min) for at least one hour prior to the heat treatment to ensure complete removal of ambient oxygen. After the heat treatment, the as-sintered samples were polished to obtain the lustrous surfaces of metallic Ti-6Al-4V. In all 3D printed-sintered Ti-6Al-4V specimens, ~27% homogeneous and isotropic volume shrinkage was recorded. Sections of 1 mm thickness were cut from the disks of Ti-6Al-4V using wire-EDM and polished further to remove the sparked surface. The thin disks were studied under a X-ray diffractometer (Rigaku, Smartlab, Japan) to investigate the phase assemblies. The 2θ scan was accomplished from 10° to 90° with a scan rate of 0.06°/s using $\text{CuK}\alpha$ radiation of wavelength 1.5418 Å.

2.7 Micro-computed tomography (m-CT)

Microcomputed tomography (VersaXRM-500, Xradia, Zeiss, Germany) analyses of 3D microstructure of Ti-6Al-4V microporous scaffolds (diameter 7~8.5 mm, 11~13 mm height) were carried out to quantitatively assess the pore size distribution, pore volume fraction and pore interconnectivities. To obtain satisfactory transmitted intensity (>5000) and transmittance at 140 kV energy and 10W power, 4X objective and different exposure times (3-7 s) were optimised for the image acquisition. In each scan, 3201 projection images were acquired at the spatial resolution of ~4 µm voxel size. Next, a number of 2D tomograms were reconstructed from the transmission images using XRM Reconstructor (Xradia, Zeiss, Germany) to obtain a virtual 3D scanned data. The scanned data were imported in Avizo Fire 8.1 (formerly FEI, France) to investigate the pore volume fraction, size distribution and pore interconnectivity. Segmentation / thresholding was carried out to binarise the image. Subsequently, the bimodal

histogram, which was obtained from the total grayscale of the data, was segmented as two different phases (material and pores). A mask was created by covering the entire grayscale values (0 ~ 65535) in the interactive thresholding. After subtracting binary image of from the mask, the corresponding volume fraction of the pore/material phase was obtained. From the imported chart of pore sizes, the closed pore size distributions and % pore interconnectivity were calculated.

2.8 Mechanical properties

Uniaxial compression test was carried out in a universal testing machine (Instron 5967 UTM, USA) using 30kN load cell and 0.5 mm/min crosshead speed (CHS). Vickers hardness was measured using a microhardness tester (FM-800, FT-Corp, Japan) equipped with square based pyramidal diamond indenter in the load range of 300 – 500 gf, imposing indent residence time of 10 seconds each. The as-sintered and polished bar specimens (~21.5mm×5mm×4.5mm, $l \times b \times d$) of Ti-6Al-4V were subjected for 3-point bending tests (14 mm span length, CHS of 0.5 mm/min) using UTM for the analysis of weakest link fracture statistics, as explained below.

Considering the presence of porosity, it was perceived that printed-sintered Ti-6Al-4V would have more brittle-like failure behaviour. Therefore, Weibull theory was utilised in the present work. The Weibull modulus (m) is a measure of the reliability of experimental strengths of brittle metallic materials. According to weakest link fracture statistics, the probability of failure can be expressed as:

$$P_f = 1 - \exp \left[- \int_V \left(\frac{\sigma - \sigma_u}{\sigma_0} \right)^m dV \right] \dots\dots (3)$$

where, P_f is the probability of failure in a certain stress, V is the volume under stress, σ is the failure stress, σ_0 is the stress at which the failure probability is 0.63, σ_u is a threshold stress

below which the failure probability is zero [7]. The failure probability of i th specimen was estimated using the following relationship:

$$P_f = \frac{n_i - 0.5}{N} \dots\dots(4)$$

where, n_i is the rank of a particular strength data ($i = 1$ is the rank of the weakest and $i = N$ for the strongest specimen) and N is the sample size (18 in this study). For the safest assumption, σ_u is considered as zero and hence the analysis turns out to be a two parameter test. Assuming uniaxial stress, we obtain the following expression for the probability of failure,

$$P_f = 1 - \exp \left[- \left(\frac{\sigma}{\sigma_0} \right)^m \right] \dots\dots (5)$$

Executing natural logarithm twice for **equation 5**, we obtain the following expression, which provides the value of the Weibull modulus (m) when plotted and fitted to a straight line,

$$\ln \left[\ln \left(\frac{1}{1 - P_f} \right) \right] = m \ln \sigma - m \ln \sigma_0 \dots\dots (6)$$

2.9 Mammalian fibroblast (3T3) and pre-osteoblasts (MC3T3) culture:

Mouse fibroblasts (3T3 Swiss Albino) cell vials were thawed and seeded in T75 flask in high glucose Dulbecco's modified Eagles medium (DMEM, Invitrogen) comprising of 4.5 gl^{-1} glucose, Glutamax, 10% foetal bovine serum (FBS, Gibco) and 1% of penicillin and streptomycin antibiotic cocktail. MC3T3 osteoblast precursor cells, derived from Mus musculus calvaria, was cultured in α -MEM (sigma aldrich) supplemented with 10% FBS and 1% of penicillin and streptomycin antibiotic cocktail (HiMedia) using the same protocol. The cells were split and were maintained using standard culturing and freezing protocols. Upon achieving 80% of confluency, the cells were enzymatically lifted using 0.25% trypsin-EDTA (1x) (Gibco). The final seeding concentration of the cells was kept as $\sim 10^4$ cells/ml for all purposes throughout the experiment.

For cells seeding, disks of inkjet printed Ti-6Al-4V samples along with the metallurgically processed and commercially available Ti-6Al-4V disks (Anand metal, Mumbai), selective laser melted Ti-6Al-4V (SLM Ti-6Al-4V, for comparative studies with osteoblasts) (INTECH DMLS, Bangalore) and glass cover slips (control) were cleaned with acetone, autoclaved and immersed in 100% ethanol for at least 12 hours. The samples were dried for another 12 hours in the culture hood under UV exposure so that no trace of ethanol was left. The surface area of the sample pellets was kept identical as of the 12mm diameter cover slips. During seeding, 2ml of cell suspension was added to a 24-well plate containing sample triplicates, to ensure that all the samples remain submerged in the cell culture media. The cells seeded Ti-6Al-4V samples were cultured in a 5% CO₂ incubator at 37°C and 95% humidity.

2.10 Picogreen assay to quantify fibroblast and osteoblast proliferation

Quanti-iT Picogreen dsDNA assay kit (Invitrogen) was used to quantify the DNA content of both the cells proliferated on different substrates following manufacturer's protocol. At each time point in culture, i.e. 2, 4 and 6 days for fibroblasts and 3, 5 and 7 days for osteoblasts, the media was removed and washed with 1x PBS followed by addition of 0.1% Triton-X for 20 min to lyse the cells. The amount of Triton-X solution was calculated according to the sample surface area (3.18 $\mu\text{l}/\text{mm}^2$). The picogreen solution was prepared by mixing of 1x TE buffer stock reagent at 1:300 dilution followed by the addition of 50 μl of lysate to the prepared reagent. After 5 minutes of incubation, the intensity was measured using multiplate reader (Eppendorf AF2200) at excitation and emission wavelengths of 485 and 535 nm. The dsDNA was quantified using a calibration curve of dsDNA (ng/ml) (concentration vs intensity, not shown here). The experiment was repeated thrice with three samples in each group during each time.

2.11 MTT assay for osteoblasts viability

The osteoblast viability on different Ti-6Al-4V specimens was determined using MTT colorimetric assay ((3(4,5-dimethylthiazol-2-yl)-2,5-diphenyltetrazolium bromide, Thermo-fisher). At each of the experimental time points (i.e. 3, 5 and 7 days), the culture medium was aspirated and the specimens were washed twice with 1X PBS. 5mg/ml MTT solution was prepared using α -MEM and added to each specimen. After 4 hrs of incubation, the tetrazolium converted to insoluble purple formazan in presence of mitochondrial dehydrogenases representing the metabolically active osteoblasts present on the Ti-6Al-4V specimens. After the incubation, dimethyl sulfoxide DMSO (Merck) was added to each well to dissolve the formazan and the absorbance was measured at 595 nm (ex) and 750 nm (em) using a microplate reader (imark, BioRad laboratories). The cell viability was calculated by comparing the absorbance value of the sample to that of control using the following relation,

$$\% \text{ cell viability} = (\text{absorbance of the sample} / \text{absorbance of control}) \times 100$$

2.12 Fluorophore tagged antibody-based staining of cytoskeletal filaments

Two sets of immunostaining, α -tubulin for fibroblasts and actin filaments for osteoblasts were performed. After 6 days (fibroblasts) and 7 days (osteoblasts) of culture, all Ti-6Al-4V samples (inkjet printed, SLM and commercial) along with the control (TCPS) with grown cells were washed twice with 1xPBS and fixed with 4% paraformaldehyde and kept for 30 min. After this, the samples were washed three times with 1X PBS, followed by permeabilization with 0.1% of tritonX. The surfaces were blocked with 1% BSA in order to prevent non-specific binding of the dye. Microtubules of the cultured cells (on inkjet printed, commercial and TCPS control) were stained using anti- α -tubulin antibodies tagged with alexafluor488 (Invitrogen) and actin filaments of osteoblasts (on inkjet printed, commercial, SLM and TCPS control) were stained using Rhodamine-phalloidin (Thermo Fischer) for 1 h.

Subsequently, DAPI (Invitrogen) was added to stain the nuclei chromatin and incubated for 15 min. The samples were finally washed with 1xPBS to remove the excess stain and the cells were observed under a fluorescence microscope (Nikon LV 100D, Japan).

2.13 Statistical analysis

All the viability and proliferation results were expressed as mean \pm standard deviation (SD). One and two tailed Student's t-tests were performed for pair wise investigations for any existing significant difference in between two groups. One-way analysis of variance (ANOVA) with post-hoc Tukey's test was chosen to investigate any existing statistically significant differences among the groups (intra and inter). SPSS-16.0 software (SPSS Inc. @2010) has been used for the analysis. The cut-off p-values were taken as $p < 0.05$ for both t-test and ANOVA.

3. Results

3.1 Ink physical properties:

The integrated methodology and the central theme of the study are described schematically in **Fig. 1a-e**. In flow sweep, the change in ink viscosity with variation in shear rate was measured, while in frequency sweep, the change in complex viscosity with variation in angular frequency was recorded (**Fig. 2a**). The static viscosity from flow sweep was measured to be ~ 2 mPa.s, while almost frequency independent dynamic viscosity having the value of ~ 16 mPa.s was noted from frequency sweep experiment. The surface tension of the ink was measured to be 55.8 mN/m. These values were further used to determine the dimensionless numbers of fluid physics for the ink during post-ejection flight and the time required for post-impact capillary infiltration. The density and pH were measured to be 1002 kg/m^3 and 7.5 – 8,

respectively. The slight basic nature of the acrylic ink is attributed to the presence of the diamine accelerator.

3.2 Ink droplets in flight: shadowgraph study and fluid physics

The diagnostic setup utilised in this study is schematically shown in **Fig. 1d**. The captured frames during the droplet flights were critically analysed and the D_{\min} , D_{\max} , D_{ave} , v_{\min} and v_{\max} values are tabulated in **Table 1**. The distribution of the droplet diameters is shown in **Fig. 2b**. Adopting the previously studied values of dynamic viscosity, surface tension, recorded velocity and diameter of the droplets, several relevant dimensionless numbers for the ink were estimated. The Reynolds number (Re), Weber number (We) and Ohnesorge number (Oh) were estimated to be 7.5, 6.44 and 0.34, respectively (see **Table 1**). The Weber number value suggests an absence of secondary breakup mechanisms (satellite droplets), further downstream of the nozzle exit plane.

3.3 Powder bed porosity and dynamic contact angle of the ink with porous Ti-6Al-4V powder bed (Washburn capillary rise)

The volume fraction of porosity (~ 0.6) in the as deposited powder bed was measured using the He-gas pycnometry. In the Washburn capillary rise experiments, the dynamic changes in the weight of the powder column with respect to time were recorded digitally from the weighing balance during the capillary infiltration. The slopes of the squared weight versus time curve for the ink and the reference liquid (hexane) were found to be $0.004 \text{ gm}^2/\text{s}$ and $0.05 \text{ gm}^2/\text{s}$, respectively (**Figs. 3a** and **3b**). Considering the contact angle, density, surface tension and dynamic viscosity of hexane as 0° , 655 kg/m^3 , 18.43 mN/m and $0.31 \text{ mPa}\cdot\text{s}$ respectively, the 'bed constant' (C_b) was calculated to be $1.57 \times 10^{-15} \text{ m}^5$. This value was further used to calculate the contact angle of $\sim 43^\circ$ for the ink in the porous Ti-6Al-4V powder bed. Such

analysis clearly indicates the hydrophilic interaction and effective wetting of the particles in the powder bed. In the calculations, the values of density, surface tension and dynamic viscosity of the ink were considered as 1002 kg/m^3 , 56 mN/m and $16 \text{ mPa}\cdot\text{s}$, respectively.

3.4 Timescale for *in situ* polymerisation: role of initiator concentration

To figure out the time window for *in-situ* polymerisation to trap powder particles, diffusing wave spectroscopy study was carried out. As a first step, the molar concentration of APS taking part in the polymerisation reaction in the powder-ink composite system was estimated. For example, while printing Ti-6Al-4V powder premixed with 2%, 4%, 6% and 8% (wt/wt) APS, the molar concentrations of APS participating in the polymerisation reaction were calculated to be 0.2M, 0.4M, 0.6M and 0.8M, respectively. For this calculation, material volume fraction in as-printed object obtained from micro-CT data, was employed. The detailed methodology to find out the molar concentration of APS in the complex powder-ink system during printing is explained in **section 4.1**.

Real time monitoring of the *in situ* polymerisation using the several concentrations of the initiator was performed quantitatively by measuring the change in the diffusion coefficients of the tracer particles in the polymerisable ink medium. The rate of decrease in diffusion coefficients of polystyrene beads in polyacrylamide solution was recorded to be slower after ~ 160 seconds (**Fig. 3c**). Linear fit to the datapoints of time-dependent diffusion coefficient, after ~ 160 seconds, reveals parallel linear regime for 0.2M to 0.6M APS. The half-life of decay for intensity correlation functions at certain time stamps of reaction are plotted in **Fig. 3d**. Interestingly, a common tendency to achieve a plateau regime was observed for each concentration, but the polymerising system containing 0.4 M APS reaches the steady state at the earliest (~ 160 s).

3.5 Phase assemblages, 3D porous architecture, mechanical properties and strength reliability

X-ray diffraction pattern of printed-sintered Ti-6Al-4V (see **Fig. S1**) exhibits the predominant presence of α -Ti (hcp) with major fingerprints at $2\theta=40^\circ$ (100% intense), 35.2° and 52.7° . The BCC Ti (β), a metastable phase at room temperature is found at the grain boundaries of the α (HCP) phase islands, as reported in our previous article [11]. Importantly, some extent of rutile formation was also noticed, which is inevitable during printing with aqueous ink system.

The segmented and volume rendered tomograms revealing pore phases, pore interconnectivities as well as pore size distributions in 3D microstructure of as-printed and sintered Ti-6Al-4V are shown in **Fig. 4**. The high resolution scan data (voxel 3-4 μm) of the thin cylindrical specimens (7~8 mm dia) were imported in Avizo Fire 8.1 and the ROI was chosen preferably from the central regions of the specimens. The predominant green/blue color in the volume rendered parallelepipeds represents a single interconnected pore, whereas smaller volumes with other colors are representatives of closed porosities. The pore volume fractions (V_p) in as-printed and sintered Ti-6Al-4V were determined to be 0.52 and 0.28, respectively. The number average pore diameters (D_n) and the pore interconnectivities (ϕ) for all the specimens are listed in **Table 2**. As expected, the number of pores is reduced 5-8 folds in the sintered specimens and the distributions were shifted towards larger pore diameters.

In order to establish the potential of inkjet printed Ti-6Al-4V for moderate load bearing implants, the mechanical properties and particularly strength reliability were measured using a host of characterisation techniques under different loading conditions. The compressive strength of ~222 MPa and modulus of ~4 GPa for the 3D inkjet printed Ti-6Al-4V were achieved. In addition, the sintered microporous Ti-6Al-4V scaffolds also exhibited average flexural strength of ~92.5 MPa and Vickers hardness of 6.2 GPa. The location/scaling

parameter (σ_0), in two-parameters analysis of weakest link fracture statistics of the flexural strength data for the sample size of 18, was found to be 98.5 MPa (**Fig. 5a**) having the failure probability of ~ 0.63 (slightly higher than the mean fracture probability, 0.5). While plotting the logarithmic data of the probabilities against the associated flexural strength information (logarithmic), it reveals the reasonably good Weibull modulus (m) of 8.1 (**Fig. 5b**), which reflects reliable strength properties of inkjet printed-sintered titanium [22, 23]. The achieved mechanical properties of as-sintered and polished Ti-6Al-4V specimens are summarized comparatively with cortical bone properties in **Table 3**.

3.6 Cytocompatibility assessments of 3D inkjet printed-sintered Ti-6Al-4V

In assessing the cytocompatibility, the mammalian (murine) fibroblasts and osteoblasts were cultured on 3D printed-sintered Ti-6Al-4V and benchmarked against control (tissue culture polystyrene, TCPS) and commercial Ti-6Al-4V (non-porous) for fibroblasts. The the same study was also performed with primary murine osteoblasts against control, commercial Ti-6Al-4V and SLM printed Ti-6Al-4V.

The MTT assay for normalised (with respect to control) cell viability studies over one week reveals the better cell viability of the osteoblasts grown on the 3DIJPP Ti-6Al-4V in comparison to the commercial and SLM counterparts (**Fig. 6a**). In each time point of culture, the cell viability on 3DIJPP Ti-6Al-4V is consistently higher than that of the control significantly ($0.05 < p$) right from day 3, while the SLM exhibits significantly higher viability only at day 7. In comparison to SLM Ti-6Al-4V, the commercial Ti-6Al-4V exhibited a better consistency towards the incremental osteoblastic viability. One-tailed Student's t-tests between the osteoblasts viabilities on SLM and 3DIJPP Ti-6Al-4V consistently show the statistically significant higher viabilities on 3DIJPP specimens in each time points (day 3, 5 and 7).

The proliferation of the cells was assessed based on quantifying DNA content at each time point of observation (2, 4 and 6 days for fibroblasts and 3, 5 and 7 days for osteoblasts), using picogreen assay. On day 2, the fibroblast cell numbers on the inkjet printed Ti-6Al-4V specimens were significantly higher than the control (**Fig. 6c**). With the progression in culture time to day 4, the cell proliferation was found to be similar on both commercial and inkjet printed Ti-6Al-4V while the scenario changed after day 6. The DNA content increased significantly on 3D printed Ti-6Al-4V compared to the control, while it was not statistically significant with respect to commercial Ti-6Al-4V specimens. An important observation was that the proliferation of the fibroblasts on the 3D inkjet printed specimens was equivalent or higher than the commercially available Ti-6Al-4V specimens throughout the entire culture timepoints.

Conforming to the observations in enhanced cell-material interaction between the fibroblasts and the 3DIJPP Ti-6Al-4V, the cytocompatibility in terms of osteoblasts proliferation was recorded in case of 3DIJPP Ti-6Al-4V in comparison to the commercial and SLM counterparts (**Fig. 6b**). While no statistically significant difference was evidenced at day 3 in between the different Ti-6Al-4V substrates, the proliferation rate of osteoblasts on both SLM and 3DIJPP was significantly higher than that of the TCPS control on day 5, while no significant difference for commercial Ti-6Al-4V. At day 7, the proliferation on 3DIJPP Ti-6Al-4V was significantly higher than that of control, whether none of the SLM and commercial Ti-6Al-4V could achieve the same. When two-tailed Student's t-test were performed in between the proliferations of osteoblasts on SLM and 3DIJPP at each time point (3, 5 and 7 days), they were found to be insignificantly ($p > 0.05$) different to each other, suggesting similar rate of proliferation of osteoblasts on SLM and 3DIJPP Ti-6Al-4V samples.

Taken together, the cellular activities of the osteoblasts are significantly pronounced on the 3DIJPP Ti-6Al-4V samples.

The augmented nature of the quantitative cytocompatibility was further validated from the enhanced cytoskeletal spreading behaviour of both the 3T3 fibroblasts and MC3T3 pre-osteoblasts on the 3D inkjet printed Ti-6Al-4V surface using antibody based staining of different cytoskeletal filaments (**Fig. 6d** and **6e**). The typical spindle like spreading behaviour of the fibroblasts on 3DIJPP Ti-6Al-4V was revealed by staining the microtubules and found to be similar in comparison with the control. In contrast, slightly elongated cell groups were observed in case of commercial Ti-6Al-4V. The rough and microporous surface of the 3D inkjet printed Ti-6Al-4V surfaces resulted in the enhanced fibroblast adhesion and spreading on the surface. The spindle shaped cell morphology observed on TCPS control and 3DIJPP Ti-6Al-4V represents the healthy and mature fibroblasts. Similar immunofluorescence technique was used to stain actin filaments to study cytoskeletal spreading of osteoblasts, which exhibit more isotropic polygonal spreading on the Ti-6Al-4V specimens (commercial, SLM and 3DIJPP) compared to the polymeric TCPS control. Although not quantified, the extent of spreading appeared to be enhanced on the SLM and 3DIJPP Ti-6Al-4V specimens compared to that of the commercial Ti-6Al-4V. While the healthy osteoblasts in **Fig. 6** were observed well spread over the ‘micro-rough’ surfaces (see **Fig. 7**) of SLM and 3DIJPP Ti-6Al-4V, the spreading behaviour (SLM and 3DIJPP) were observed to be pretty much similar.

In the order of these observations, it can be argued that both the cell lines are metabolically healthy and are in well proliferative state on the 3D inkjet printed Ti-6Al-4V, which is equivalent or better in comparison with the TCPS control, commercial and SLM Ti-6Al-4V at each culture timepoint. To better probe the origin of the good cytocompatibility results, surface wettability and average surface roughness were also investigated. An

interesting trade-off between surface topography and mechanical properties was observed, where both the 3D inkjet printed ($R_a \sim 8.5 \mu\text{m}$, $CA \sim 85^\circ$) and SLM Ti-6Al-4V ($R_a \sim 11.5 \mu\text{m}$, $CA \sim 58^\circ$) exhibited two orders of magnitude higher surface roughness than commercial Ti-6Al-4V ($R_a \sim 0.1 \mu\text{m}$, $CA \sim 51^\circ$), leading to higher contact angle. The mechanical properties possessed by the 3DIJPP Ti-6Al-4V is around 1.5 order less than those of commercial and monolithic SLM Ti-6Al-4V. The results of the surface roughness and the resulting contact angle with distilled water are represented in **Fig. 7**.

4. Discussion

In this section, we shall critically analyse the adopted processing approach and its impact on the 3D microstructure, mechanical and cytocompatibility properties of 3D inkjet printed biomaterial with Ti-6Al-4V as a model system. Till date, ink in 3DIJPP is used in two modes – indirect and direct. The indirect mode involves the mixing of starch/ water soluble polymer (e.g. PVA, maltodextrin etc.) with biomaterial powder and subsequently printing with distilled water. In contrast, direct mode involves the use of a water soluble adhesive ink. The green strength and print resolution are limited in case of ‘indirect’ printing. The high viscosity of adhesive ink, used in ‘direct’ mode of printing results in frequent clogging of micro-nozzles. To resolve these twin catches, a hybrid ink system has been invented in the current study, where the binding is achieved by allowing *in situ* room temperature polymerisation reaction in the powder bed itself. The printable powder was modified with a persulfate initiator, which was subsequently printed with an aqueous acrylic monomer solution added with a diamine accelerator. The polymer chains grow locally in the micro-impact zone of droplet-substrate, thereby trapping the powder particles intimately.

The dimensionless numbers (Reynolds, Weber, Ohnesorge) of fluid physics for the ink were determined to endorse the ‘inkjet printability’. Furthermore, the timescale for the

evolution of macromolecules during *in situ* polymerisation in effectively restricting/binding micro-tracer particles was analysed using diffusing wave spectroscopy (DWS). For the first time, DWS was used as an analogous system to find out the time required for powder particles to be bound by the *in situ* polymerisable ink during inkjet powder printing. Washburn and Carman models for fluid penetration in porous media were extensively used to determine the timescale for the infiltration of the ink in the porous powder bed under capillary force. Such calculations emphasize that the time elapsed between two layer depositions (in the order of seconds) should not overwhelm the time required for polymerization (in the order of minutes), at the same time should be higher than the time window required for trans-layer capillary infiltration (in the order of milliseconds).

4.1 Unique ink system for 3D inkjet powder printing

The major advantages of free radical polymerisation/addition polymerisation are known to be the fast reaction rate and relative insensitivity towards monomer impurities. Additionally, less rigorous reaction conditions and the applicability of ambient reaction temperature are the additional benefits[24]. The schematic of the acrylamide polymerisation in the presence of APS and TEMED is shown in **Fig. S2**.

In our novel approach, the printable powders are modified with APS. As acrylamide monomer solution is sprayed 'on demand' on the powder layer during printing, the polymerization reaction is initiated, leading to rapid increment in viscosity locally. This results in an intimate adhesion of adjacent powder particles. As stated earlier, an effort to derive the molar initiator concentrations in a powder-ink complex environment is exerted herewith. These concentrations of APS were utilised to track the *in-situ* polymerisation reaction in DWS study to figure out the time required to enable the polymerising ink system

for effective trapping of tracer particles. An example for the derivation of molar concentration of APS in powder-ink composite system is explained below.

Now, we shall consider the case of Ti-6Al-4V powders pre-mixed with 4 wt% (wt/wt) APS. The volume of ink dispensed to print 1 ml volume of CAD was 0.86 ml (information retrieved from printing software, total ink volume dispensed divided by the CAD volume). From micro-CT data, the 'material volume fraction, V_m i.e. $(1-V_p)$ ' of as-printed Ti-6Al-4V green body was determined to be 0.47. In other words, 0.47 ml of Ti-6Al-4V powder is present in 1 ml printed CAD volume. Therefore, the corresponding weight of Ti-6Al-4V would be 2.07 g (0.47×4.4 ; considering the density as 4.4g/cc). As a result of 4% wt/wt mixing, the content of APS stands out to be 0.08 g in 2.07 gm Ti-6Al-4V. At this point, one can very well perceive that, 0.86 ml ink (22% aqueous acrylamide solution with 2% TEMED) interacted with 0.08 gm APS during the printing. From this, the molarity of APS can be calculated in the ink system to be 0.41M. Similarly, one can calculate the molar concentrations for 2%, 6% and 8 % (wt/wt) APS in Ti-6Al-4V powder, which should be 0.2 M, 0.6M and 0.8M, respectively. Reiterating, this is an example for a comprehensive understanding of the procedure to calculate the effective initiator concentration taking part in the reaction, which in general, can be adopted for other powders, initiator and monomer solution combinations.

The dynamic viscosity is the measure of the resistance experienced by the adjacent layers of the flowing liquid. A frequency independent dynamic viscosity signifies the laminar flow, which should be the characteristic of an ink for inkjet printing. The dynamic viscosity value (~ 16 mPa.s) for the novel ink lies well in the prescribed range for inkjet printing (30 mPa.s)[25] As the ink is non-adhesive prior to interaction with initiator added powder

particles and the static viscosity value is considerably low (~ 1.8 mPa.s), it endorses the safe and uninterrupted printability incurring no nozzle/micro-orifices clogging.

The surface tension plays a vital role in ejection and flight of ink droplets. In case of low surface tension, the liquid wets the outer nozzle surface, followed by gradual accumulation to form larger drop. This can not only potentially degrade the print resolution, but also, the lower surface tension encourages the generation of larger satellite droplets to affect the print resolution further[26]. In case of higher surface tension, the ability to spread and to wet the powder bed will be less, resulting in poor bonding. The aqueous ink exhibits a legitimate surface tension of 56 mN/m, which is well below that of distilled water (~ 72 mN/m).

4.2 Fluid physics of ink, *in situ* shadowgraphy

The dimensionless numbers of fluid physics govern the physico-mechanical properties of ink under flight. The Reynolds number ($v\rho a/\eta$) depicts the ratio between inertial and viscous forces, Weber number ($v^2\rho a/\gamma$) represents the ratio between kinetic energy and surface energy. Also, Ohnesorge number ($\eta/\sqrt{\rho a\gamma}$) describes the relative importance of viscous and surface forces where, v , ρ , γ , η and a are droplet velocity, density, surface tension, viscosity and characteristic length (droplet diameter), respectively[27]. The ejection velocity, droplet diameter and surface tension (pendant drop) from shadowgraphy and dynamic viscosity from cone plate viscometry (frequency sweep) were implemented to quantify the dimensionless numbers of the ink. As well explained in literature, the value of Oh and Re should lie in the ‘Printable fluid’ region of **Fig. 2c**, i.e. in the range of 0.1 – 1.0 and 5 – 100 respectively which in turn dictate stable drop formation and optimum inkjet printability [28]. According to a numerical simulation by Reis et al, value for Z ($1/Oh$) should be in the range of $1 < Z < 10$ for stable drop generation [29]. Viscous dissipation would prevent drop ejection if $Z < 1$ and for

$Z > 10$, satellite droplets would generate accompanying the parent droplets, degrading the print resolution [25, 29]. The value of Z for the novel ink was found to be ~ 3 . The quantification of the physico-mechanical characteristics for the ink rationalises the efficacy of high quality inkjet printing, independent of powder chemistry.

4.3 Washburn capillary rise

The synchronisation of several phenomena or parameters during 3D inkjet powder printing, e.g., powder layer deposition speed, capillary infiltration of ink in between the adjacent loose powder layers and subsequent *in-situ* polymerization, determine the mechanical robustness of 3D-printed solids. This largely depends on the effectiveness of the wetting of powder particles by the ink. To study the capillary infiltration time during printing, we adopted the Washburn and Carman models for fluid flow in porous media. One of the important parameter to study the same for a set of powder and a liquid is the dynamic contact angle of the particular liquid on the surface of the powder particles. It is quite obvious to realise that the measurement is not as straight forward as one can carry out on a flat solid substrate with a liquid drop in sessile mode. Washburn capillary rise (WCR) is an established technique to measure the contact angle of flowing liquid through a porous powder column. Bell and Cameron[30] experimentally established a linear relationship between square of the length penetrated and the time required for the penetration during infiltration of a liquid through a capillary. Later, Washburn came up with the theoretical foundation to prove the above experimentation, where the constant for the squared distance and the time ratio depends on diameter of the tube, surface tension, dynamic viscosity of the liquid and the contact angle with the capillary wall [31]. Washburn's constant (W_c) relating the penetration length (l) and time (t) can be expressed as,

$$W_c = \frac{l^2}{t} = \frac{D_{tube}}{4} \frac{\gamma}{\eta} \cos\theta \quad \dots\dots(7)$$

where, D_{tube} , γ , η and θ are capillary diameter, surface tension, viscosity and contact angle respectively. The mass of a liquid contained in a capillary can be expressed in terms of the capillary diameter (D_{tube}), length penetrated by the liquid (l) and the density (ρ_l). The mass of the penetrated liquid can be expressed in terms of the above parameters as,

$$M = \frac{D_{tube}^2}{4} l \rho_l \quad \dots\dots(8)$$

Putting the expression of l in **equation 7**, one can obtain the following relationship,

$$\frac{M^2}{t} = \frac{\pi^2 D_{tube}^5}{64} \frac{\rho_l^2 \gamma}{\eta} \cos\theta = C_b \frac{\rho_l^2 \gamma}{\eta} \cos\theta \quad \dots\dots(9)$$

where C_b is known to be the bed geometric constant, independent of the liquid type if the powder bed is uniform and reproducible[15]. As the porous bed can be considered as a bundle of capillaries, the bed constant is only dependent on the effective diameter (D_{tube}). As the value of the geometric constant is dependent on the fifth power of the effective diameter, the experiment is highly sensitive to the powder bed reproducibility. To ensure this, the centrifugal packing methodology was adopted to reproduce the bed packing. The robustness of the above theoretical calculation was established by using two different liquids so that the perceived influence of porosity on bed constant (C_b) can be ignored. For example, the bed constant and porosity will vary depending on the packing density, but the effect will be exactly alike for both liquids. Hence, the above approach does not leave any effect on the contact angle of the liquid under interest. As the bed packing and porosity are different in 3D printing bed and centrifuged bed, the two-liquid technique was comprehended to be effective to find out the dynamic contact angle of the ink in porous powder bed.

4.4 Theoretical calculation of capillary infiltration time

In this section, we have adopted a theoretical methodology to quantify the timescale for the ink to infiltrate a single powder layer deposited during 3D powder printing. Washburn and Carman models were applied for the theoretical estimation of the capillary infiltration time for a 100 μm thick powder layer[31, 32]. After the ink droplets arrive at the powder bed, three consecutive transient phenomena set out as, impact driven stage, capillary infiltration and equilibrium attainment (*in situ* polymerization). In the following section, quantitative derivations for effective capillary radius, capillary pressure and tortuous capillary lengths are carried out. These derived quantities will be successively applied to figure out the single layer infiltration time using Washburn model.

4.4.1 Effective capillary radius (r) of porous bed

In the following theoretical calculation, APS modified Ti-6Al-4V powders having D_{32} of $\sim 14 \mu\text{m}$ was considered. The SEM images of the powders before and after modification are shown in **Fig. S3**. Hydraulic diameter (d_H) is defined as the ratio of volume and surface area of pores for a porous bed. The porosity (p) of a porous bed is related to the hydraulic diameter as,

$$d_H = \frac{p}{(1-p)} \frac{D_{32}}{6} \dots\dots\dots(10)$$

We obtained the value of porosity (p) as 0.6 from He-gas pycnometry of as-deposited Ti-6Al-4V bed giving rise to the value of hydraulic diameter of the porous bed (**equation 10**) to be $\sim 3.5 \mu\text{m}$. The effective capillary radius (for a circular capillary) is therefore $\sim 7 \mu\text{m}$ (capillary radius is twice that of its hydraulic diameter, one should not be confused with the conventional relation between radius and diameter). Therefore, the capillary rise physically takes place in a narrow constricted region of spatial dimension of around $7 \mu\text{m}$. As shown in

Table 2, the average pore size in as-printed scaffold is 8.9 μm which is well in the range of the calculated one. The above discussion explains the significance of powder particle size on the effective capillary radius for infiltration.

4.4.2 Capillary pressure (P_c) of porous bed

The capillary pressure (P_c) in the bed has been estimated to determine capillary infiltration time. For the event of capillary rise, capillary pressure difference (ΔP_c) is related to surface tension (γ), effective capillary radius (r), contact angle (θ), density (ρ), gravity (g) and vertical capillary height (h) as,

$$\Delta P = \frac{2\gamma}{r} \cos\theta - \rho gh \quad \dots\dots\dots(11)$$

In 3D powder printing, the capillary flow is in the direction of gravity and therefore, the negative sign in the above stated expression will be additive in nature. Interestingly, as we see later, the gravity assisted pressure is negligible compared to the capillary pressure. For example, the quantity, ρgh obtains the value of 0.98 Pa ($h = 100 \mu\text{m}$), whereas the capillary pressure values assume the value in the order of kPa. Putting the values of surface tension, effective radius and contact angle in **equation 11**, one can obtain the capillary pressure difference in the powder bed as ~ 11.7 kPa. Such pressure difference aids in effective ink infiltration and simultaneous wetting of powder particles during printing. This analysis will be further used to estimate the timescale of infiltration in a later subsection.

4.4.3 Tortuous capillary length (l_T) of a thin powder layer

The capillary path for liquid ink to travel through a powder bed is never linear and in reality, highly tortuous in nature. Carman suggested that the tortuous path length is $\sqrt{2}$ times that of the vertical length [32]. For the capillary path through a simple close pack arrangement of

spherical powder particles (see **Fig. 8**), the ratio between the tortuous and the vertical distance (l_v) between plane MM and NN are deduced. From the simplistic geometric analysis, the vertical distance between plane MM and plane NN is $3.73r$.

$$l_v = (2 + AB \cdot \tan 60^\circ) \cdot r = 3.73r$$

Now, let us find out the tortuous distance (l_t) between these two planes. The cumulative length of *arc AD*, *arc AE*, *arc EF* and *arc FG* of the two circles centered at point B and C, is the tortuous length the ink travels in real space,

$$\text{arc}AD = r \cdot \left(\frac{\pi}{3}\right) = 1.05r; \quad \text{arc}AE = r \cdot \left(\frac{\pi}{2}\right) = 1.57r$$

The path contribution from one sphere is therefore $2.62r$. For a thick layer with two such packed layers of spherical particles, the value will be $5.24r$. Now the liquid ink reaches the plane NN from plane MM. Finally, the ratio between the two distances comes out to be $(5.24/3.73) \sim 1.41$ or $\sqrt{2}$. Therefore, the actual tortuous length that the ink will travel through powder layer is $\sim 141 \mu\text{m}$ ($100 \times \sqrt{2} \mu\text{m}$). Such analysis is useful to understand that the tortuous path length a stream of ink travels is considerably higher than the particular thickness of the powder layer displaced during powder-ink interaction.

4.4.4 Time of infiltration using Washburn model

The time required (t) for liquid penetration through a series of vertical capillary channels depends on the effective capillary radius (r), friction coefficient of the liquid on the wall (ϵ), density (ρ), dynamic viscosity (η), capillary pressure (P_c) and the penetrated length (l). The capillaries in the porous powder bed can be considered as open capillaries in both sides. In this case, the atmospheric pressure can be neglected in the analysis of infiltration time. According to Washburn, the expression of time related to the other parameters can be expressed as,

$$\frac{(r^2 + 4\epsilon r)\rho \cdot g}{8(\eta - \eta_A)} t + l = \frac{-(\eta - \eta_A)\left(\rho \cdot g \cdot h + \frac{2\gamma}{r} \cos\theta\right) + \rho \cdot g \cdot \eta_A l_T}{\rho \cdot g \cdot (\eta - \eta_A)} \cdot \log_e\left(1 - \frac{\rho \cdot g \cdot l}{\rho \cdot g \cdot h + \frac{2\gamma}{r} \cos\theta}\right) \quad \dots\dots(12)$$

where, η_A and l_T are the dynamic viscosity of air and the total length to be penetrated. As we are interested in the total travel time for the actual tortuous length through the thickness of 100 μm , l can be replaced by l_T . Assuming the absence of interfacial friction (ϵ) between the liquid and the particle walls, the modified form of the **equation 12** is,

$$\frac{r^2 \cdot \rho \cdot g}{8(\eta - \eta_A)} t + l_T = \frac{-(\eta - \eta_A)\left(\frac{2\gamma}{r} \cos\theta\right) + \rho \cdot g \cdot \eta_A l_T}{\rho \cdot g \cdot (\eta - \eta_A)} \cdot \log_e\left(1 - \frac{\rho \cdot g \cdot l_T}{\frac{2\gamma}{r} \cos\theta}\right) \quad \dots\dots(13)$$

Using the expression for the capillary pressure P_c as $(2\gamma/r) \cos\theta$, we obtain,

$$\frac{r^2 \cdot \rho \cdot g}{8(\eta - \eta_A)} t + l_T = \frac{-(\eta - \eta_A) \cdot P_c + \rho \cdot g \cdot \eta_A l_T}{\rho \cdot g \cdot (\eta - \eta_A)} \cdot \log_e\left(1 - \frac{\rho \cdot g \cdot l_T}{P_c}\right) \quad \dots\dots(14)$$

Putting the values of $r = 7 \mu\text{m}$, $\rho = 1002 \text{ kg/m}^3$, $g = 9.8 \text{ m/s}^2$, $\eta = 16 \text{ mPa}\cdot\text{s}$, $\eta_A = 0.8 \text{ mPa}\cdot\text{s}$, $l_T = 141.4 \mu\text{m}$ ($100 \mu\text{m} \times \sqrt{2}$) and $P_c = 11.7 \text{ kPa}$ in equation 14, one can obtain the infiltration time for 100 micron thick layer to be $\sim 150 \text{ ms}$.

After this stage, the infiltrated ink will remain in equilibrium for up to 8 seconds, which is the maximum residence time before the deposition of next layer (printing speed ~ 7 layers/min). Therefore, the residence time is two orders of magnitude larger than the infiltration time. This would allow the ink to infiltrate properly through the thickness of the powder bed. At this stage, *in-situ* polymerisation will initiate and propagate to trap/bind the surrounding powder particles in accordance with the on-demand CAD patterns. In the next section, in reference to the outcomes of the DWS study, the time required for the particle trapping as a result of *in situ* polymerisation will be quantitatively discussed.

4.5 Real time monitoring of simulated powder-binder interaction

The *in situ* polymerisation assisted powder particle binding during inkjet printing is now perspicuous in the backdrop of the discussions in the antecedent sections so far. A conventional polymerising system consisting of monomer solution, initiator, accelerator and micro-particles was conceptualized experimentally as a simplistic analogue to model the *in situ* particle trapping by the macromolecules during 3D inkjet powder printing. To achieve this, diffusing wave spectroscopy (DWS) was employed to monitor the changes in microrheological properties of the ink system during *in situ* polymerisation and the onset of successive particle trapping in real time[33]. The schematic of the experimental set up is shown in **Fig. S4**. Particularly, the viscous macromolecule formation during the free radical polymerisation process can be perceived by analysing time dependent diffusion coefficient of polystyrene micro-beads in the acrylamide solution medium in different time intervals. As expected, the time dependent diffusion coefficient values decrease with initiator concentration. This results in trapping of polystyrene beads, which reflects the slower diffusivity of beads in polyacrylamide system. After ~160 seconds, the diffusion coefficients for all concentrations exhibited nearly time independence (**Fig. 3c**). This clearly signifies the time window of ~160 seconds to be sufficient to form a strong polymer network to restrict the micron-sized tracer particles. It implicates that, at around 160s, nascent polymer molecules are capable to bind with the micron sized particles (e.g. Ti-Al-4V particles during inkjet printing) present in the polymerisation system. Similar behaviour of polymerization reaction kinetics for 0.4M and 0.6M APS concentration can be noted from parallel linear regime of time dependent diffusion coefficient of embedded tracer particles in the polymerizing ink medium.

When molecular motion in the system is high, i.e. the scope and duration of interactions of the laser light with the particle is less, the intensity correlation function decays

faster (see **equation 1**). In contrast, the decay is expected to be slower through a macromolecular system. It needs to be emphasized here that half decay time (τ) essentially denotes the residence time of photons in the medium before being transmitted out from the cuvette. In this perspective, it can be argued that, the half-life of decay correlates directly with the propagation of the free radical polymerisation, leading to dynamic increment in viscosity[20]. The onset of the plateau region in the half decay time curve was found to be earliest in case of 0.4M APS signifying the effectiveness of 4 wt% APS modified Ti-6Al-4V powder for a steady, yet reasonably faster *in situ* polymerisation.

4.6 Phase assemblage and 3D microstructure of inkjet printed and sintered Ti-6Al-4V

The working principle of 3DIJPP is based on the on-demand delivery of aqueous ink to a powder bed. After 3D inkjet printing, the printed parts are heat treated at high temperature in argon atmosphere. Subsequently, they were characterised using XRD, SEM and micro-computed tomography techniques. In addition, specific mechanical properties were quantitatively assessed. Although titanium is highly sensitive towards oxidation, a thin protective oxide layer on the surface prevents the oxidative corrosion. At high temperature, the thin oxide layer dissolves in Ti matrix and contributes in additional strengthening and hardness. The evolved rutile phase, as detected by XRD analysis is known to be biocompatible and contributes in enhancing the hardness of sintered Ti-6Al-4V[34-36].

The in depth 3D porous microstructure analysis was conducted to quantify the pore volume fraction, pore interconnectivity and closed pore size distribution of the as-printed and sintered specimens. The solid state diffusion assisted mass transport during sintering along with the adjacent grain boundary fusions resulted in closing up the pore channels in the green bodies. As a result, the interconnectivity was reduced in all as-sintered specimens (see **Fig.**

S5). As expected, the pore volume fractions were decreased after sintering. In the volume rendered pore phase images, the discrete multicoloured tiny objects (**Fig. 4b**), scattered randomly in 3D, essentially represent the close porosities. The closed-pore size distributions exhibit the nature of porosities in as-printed and as-sintered specimens. In line with the prediction, the number of closed pores is reduced 5 – 8 folds after sintering, as observed from the pore-size distribution curves. Interestingly, the pore size distributions shifted rightward (higher diameter side) in sintered Ti-6Al-4V. This can be rationalised from the perspective that, the pore volume fraction and pore numbers were decreased at the cost of increment in the pore diameters due to coalescence of small pores in the ‘triple pockets’. The lower ends of the pore size distributions were voxel size limited (3 – 4 μm), below which the pores remained undetected in micro-CT analysis. Apart from the fact that the intrinsic process-generated interconnected microporosities (<100 μm) are extremely helpful in physiological liquid exchange, nutrition supply and metabolic waste removal, these 3D microstructural elements assist in efficient protein absorption in culture media leading to cell colonisation *in-vitro*. To facilitate neo-vascularisation and bone regeneration, designed macroporosities has to be incorporated in the CAD design, which was demonstrated in one of our previous article [1, 11, 37]. It is worthy to mention that, to justify the term ‘non-porous solid’ to describe the metallurgically processed commercial Ti-6Al-4V in this manuscript, a similar 360° micro-CT scan was also performed for the commercial Ti-6Al-4V as well, using the same tomography recipe, to evidence the absence of any porosity in the monolithic microstructure (**Fig. S6**). The similar 3D volume rendered non-porous microstructure of the SLM manufactured Ti-6Al-4V specimen is also provided accordingly from literature[38].

4.7 Mechanical property and strength reliability

The combination of compressive strength, flexural strength and hardness values for 3D inkjet printed Ti-6Al-4V was found to commensurate well with the mechanical properties of human cortical bone (see **table 3**). The strength and modulus achieved for Ti-6Al-4V constructs manufactured using different AM technologies involving both binder jetting and powder bed fusion based non-porous architectures are summarised in **table 4** [11, 38-43]. It was well observed that, the compressive strength and modulus recorded in binder jetting methodology are closely comparable with those of the human cortical bone. The properties of natural cortical bone were obtained from published literature [44-50]. The sintered microporous Ti-6Al-4V specimens exhibited the biomedically significant flexural strength (92.5 MPa), which was well in the regime of human cortical bone (50 – 150 MPa) [51-53]. An augmented Vickers hardness value of 6.2 GPa was measured with 3D powder printed microporous Ti-6Al-4V. The presence of rutile in the microstructure of α - β Ti-6Al-4V is suspected to be responsible for the increment in the hardness of as-sintered Ti-6Al-4V. As the specimens are microporous, the stress-strain responses of the specimens exhibited brittle failure, as expected (see **Fig. S7**). Conceiving the knowledge of the micro-porosities (~28 vol%) present in the sintered Ti-6Al-4V models, which are the deliberate occurrence of flaws in the microstructures; it should be of high priority to assess the mechanical strength reliability of the specimens in real scale loading conditions. This is the first endeavour ever reported in the literature to gain an insight into the strength reliability of 3D inkjet printed metallic samples. On the basis of weakest link fracture statistics (two-parameter), the thresholding value of stress (σ_{ii}) was assumed to be zero, i.e. any minimum stress is sufficient to initiate the overall structural failure[54, 55]. From the obtained data of the micro-CT based 3D microstructural analysis, it is quite apparent that the interconnected micro-porosities are homogeneously

distributed along the overall volume of the sintered specimen, thereby providing the logical platform for the above-mentioned assumptions for the statistical analysis of strength reliability. Linear regression analysis was used to fit the data to obtain the Weibull modulus. Tiryakioglu et al. used Monte Carlo simulation to figure out the critical points of R^2 and recommended the following method to evaluate the robustness of the fit for sample size between 5 and 100[22, 56].

$$R_{0.05}^2 = 1.0637 - \frac{0.4174}{n^{0.3}} \dots\dots (15)$$

In case, the value of R^2 being higher than $R_{0.05}^2$, the two parameter Weibull analysis is reliable and on the contrary, the analysis can not be considered as valid if R^2 is less than $R_{0.05}^2$. For a sample size of 18, the $R_{0.05}^2$ value turns out to be 0.89 which is well below the R^2 value (0.97) in the case of 3D inkjet powder printed Ti6Al4V specimens. While correlating properties with microstructure, it appears that highly interconnected 3D porous architecture of inkjet printed Ti-6Al-4V contributes towards reliable strength properties.

4.8 Cell-material interaction

In this section, an attempt has been made to rationalise the results of cell-material interaction exhibited by the 3D inkjet printed Ti-6Al-4V specimens with different cell lines, murine fibroblasts and primary osteoblasts. Apart from the robust theoretical and experimental foundations of the novel processing approach, it is believed to be the first ever report in the literature to extensively study the cellular response on inkjet powder printed metallic biomaterials with two cell lines. When an implant as a foreign body is introduced in body environment, it gets exposed immediately with the connective tissue and bone cells, which majorly constitute the host tissue to interact with the implant or scaffold. This is the central rationale behind the strategic selection of mammalian fibroblasts and primary osteoblasts for

in vitro cultures of 3DIJPP Ti-6Al-4V specimens, our results are benchmarked against metallurgical processed and SLM Ti-6Al-4V[57-59]. It is well known that the cellular structural environment, topography and mechanical properties directly influence the cell adhesion, proliferation and most often differentiation, depending on the cell types[60-66]. As confirmed from the micro-computed tomography, 3D microstructures of the printed-sintered Ti-6Al-4V comprise of highly interconnected micro-porosities. From biocompatibility aspect, ~98% interconnected porosity in the printed-sintered architectures is extremely beneficial in ‘assisting’ tissue in-growth[11, 67, 68].

We shall now make an attempt to explain the cytocompatibility results on the basis of the relevant physical properties. From **Fig. 7**, the interplay among the contact angle and the average surface roughness can explain similar or even better cellular response on 3D printed-sintered Ti-6Al-4V, when compared to the SLM and commercial counterpart. The surface wettability influences the efficacy of the protein absorption, prior to the neutrophil interrogations and subsequent cell adhesion. By virtue of slower heat treatment compared to SLM, pore aggregation and pore island embedded in otherwise smooth metallic surface is the characteristic feature of 3D inkjet printed-sintered Ti-6Al-4V morphology. This also explains lower average surface roughness compared to SLM (**Fig. 7**). Due to rapid melting and superfast cooling involved in SLM based 3D printing of Ti-6Al-4V, the particles get more or less ‘frozen’ in their original location. As a result, the distribution of the micro-peaks and valleys is more homogeneous in case of Ti-6Al-4V prepared in SLM route. Also, the R_a value is higher in case of SLM Ti-6Al-4V. Although higher contact angle is witnessed in case of rougher surface, the liquid-solid contact angle does not depend solely on average roughness value. In fact, it depends on the nature of porosity distribution as well, where surface wetting may be more pronounced (less contact angle) in case of homogeneously porous surface (SLM)

in comparison to a surface with a distributed composite of smooth surface and porosity islands (3DIJPP). Although the contact angle for 3D inkjet printed Ti-6Al-4V was higher compared to the control, commercial and SLM Ti-6Al-4V, the high surface roughness, 3D pore interconnectivity and reduced stiffness indeed mediated equivalent cell adhesion and spreading behaviour in comparison with SLM, and better when compared to the commercial counterpart (**Fig. 6e**) [69-76]. The rough porous islands (interconnected in 3D), as observed in the surface profile of inkjet printed Ti-6Al-4V (**Fig. 7**) averment the abundance of probable sites for focal adhesion complexes leading to better cell attachments (**Fig. S8**). The effect of surface roughness on cell adhesion and spreading is evident from **Fig. 6** qualitatively, where the fibroblasts and osteoblasts experience enhanced spreading on the 3DIJPP and SLM surfaces having a very high surface micro-roughness (8–12 μm) compared to the commercial Ti-6Al-4V (0.1 μm). Not only limited to the rough surface and porous nature of the scaffolds, an inevitable beneficial outcome of the 3D interconnected porous architecture of the 3DIJPP Ti-6Al-4V is the almost 1.5 order of magnitude lesser elastic modulus, in comparison with the commercial and SLM counterpart[38, 42]. The matrix stiffness is known to regulate cell behaviour, motility and differentiation. It is well reported that, cells always tend to migrate and attach on the matrix having lower stiffness[65, 77-80]. The consistently higher osteoblasts viability on the 3DIJPP Ti-6Al-4V substrates compared to the SLM counterpart, demonstrates the beneficial aspects of interconnected 3D porous microstructure and reduced modulus favouring the bone cell activities. The proliferation of the osteoblasts were observed to be similar on both SLM and 3DIJPP Ti-6Al-4V (insignificant difference from Student's t-test) which was further supported by the fluorescent images of the cytoskeletal spreading behaviour (**Fig. 6e**). Together with the cell viability (osteoblasts), immunofluorescence based staining of the α -tubulin of fibroblasts and actin filaments of osteoblasts to probe the cytoskeletal

spreading behaviour, the proliferation assay in terms of DNA quantification (for both fibroblasts and osteoblasts) clearly depicts the inflexibility of the novel processing approach towards the uncompromised cytocompatibility of pristine Ti-6Al-4V [81, 82]. The increased expression of fibronectin around the receptor proteins of the fibroblasts adhered to 3DIJPP Ti-6Al-4V substrates and long term metabolic status of the cells with targeted calcium activity (explained in supplementary section with **Fig. S8** and **Fig. S9**) also supports the augmented cytocompatibility of the novel processing strategies to manufacture Ti-6Al-4V based implant and scaffolds.

While there is always a trade-off among the porosity, permeability and mechanical properties, 3D inkjet printing provides us an opportunity to tailor the same to achieve the optimum biocompatibility properties for implantable biomaterials. The pore size distribution and volume fraction of pores together influence the permeability of nutrients, metabolic waste removal and tissue ingrowth. It is therefore essential to maintain the balance among the pore volume fraction, size distribution and specific surface area for optimal cell migration and attachment [83-86]. For uncompromised biocompatibility, implants having the first two attributes are believed to be the gold standard together with strength reliability of porous implant.

Looking at the broad horizon of the technology space, this high throughput scalable technique together with the novel ink system and our present understanding of the process strategy, is expected to expand the scope of 3DIJPP to compete with traditional and laser-based additive manufacturing of metals. A number of small and medium enterprises currently employ 3DIJPP for commercial production of complex aerospace components, mould toolings, automotive engine parts, turbine blades for energy conversion and complex short series productions. All those components are normally used in the fully dense solid format. For

example, Desktop Metal™, a Massachusetts (USA) based company, emerged in 2015 as a R&D based metal inkjet printing solution for the industry scale productions of engineering components, particularly inkjet manufacturing of steel parts [87]. The binder jetting technology in 3D inkjet powder printing is also commercialised by HP™ very recently (2018) in their ‘Metal Jet’ technology to manufacture metallic parts with industrial scale and high volume[88]. Against the backdrop of the present work to adapt 3DIJPP to produce porous Ti-6Al-4V, we expect this study will have significant impact on the manufacturing of metallic implants in near future.

5. Conclusions

The present work has established the experimental and theoretical foundation of 3D inkjet powder printing based manufacturing of metallic biomaterials. In particular, a new process pathway involving strategic modification of powders with printable ink formulation has been adapted to demonstrate the role of *in situ* polymerisation on the effectiveness on powder-ink interaction in the context of ‘printability’. More importantly, we presented an integrated approach by employing the theoretical models together with experiments to analyse capillary infiltration as well as real time monitoring of *in situ* polymerisation. With commercially available biomedical grade Ti-6Al-4V powder as a model biomaterial, we have demonstrated the range of reliable mechanical properties with 3D porous microstructures using our new process protocol and such spectrum of properties is comparable to that of natural human cortical bone. When benchmarked against commercial and SLM Ti-6Al-4V (non-porous), 3D inkjet printed Ti-6Al-4V exhibited favourable cellular responses in terms of both fibroblast and osteoblast cell viability, cytoskeletal spreading and proliferation, *in vitro*. Cell-biomaterial interaction was further explained via an interplay of elastic stiffness, surface roughness and wettability. Although the wettability on the SLM Ti-6Al-4V surface was higher, it was found that the holistic effect of layered interconnected microporosity, reduced stiffness and

relatively lower surface roughness favoured 3DIJPP Ti-6Al-4V to exhibit equivalent osteoblast spreading and proliferation but higher viability than SLM Ti-6Al-4V.

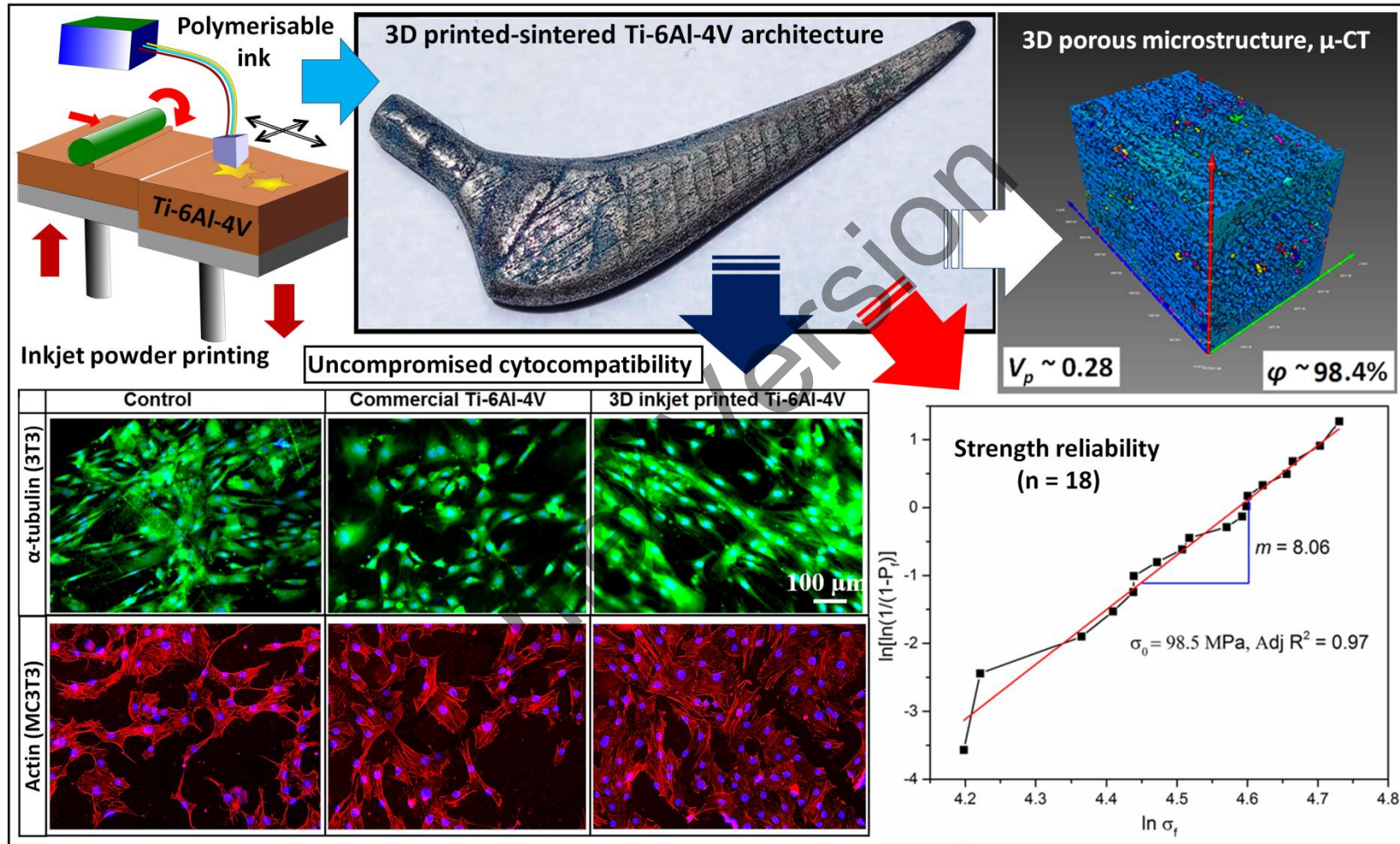
At the closure, this study has unveiled a better quantitative understanding of inkjet powder printing as step-by-step and an adaptable additive manufacturing process for metallic biomaterials with reliable mechanical properties and cytocompatibility, thereby overcoming the long standing ‘black box’ approach.

Acknowledgements

The authors would like to convey special thanks to Prof. Jayadeep K. Basu, Dr. Kaushik Chatterjee, Dr. Suryasarathi Bose, Dr. Mrinmoy De (IISc, India) and Dr. Subhadip Bodhak (CGCRI, India) for their valuable suggestions and supports and also thank Mr. Sashi Dhara, Mr. Sourav Mandal, Ms. Vidushi Sharma, Ms. Swati Sharma (IISc, India), Mr. Satish Jaiswal (IITR, India), Dr. Vimal Kumar (IITKGP, India) and Dr. Aniruddha T. Jagannath (Ramaiah Memorial Hospital, Bangalore, India) for their valuable suggestions and comments.

The authors would like to further acknowledge Department of Science and Technology (DST), Department of Biotechnology (DBT) (grant No. BT/PR13466/COE/34/26/2015), Government of India, and Centres of Excellence and Innovation in Biotechnology – ‘Translational Center on Biomaterials for Orthopaedic and Dental Applications’ for financial supports.

Table of Content (TOC)



List of figures:

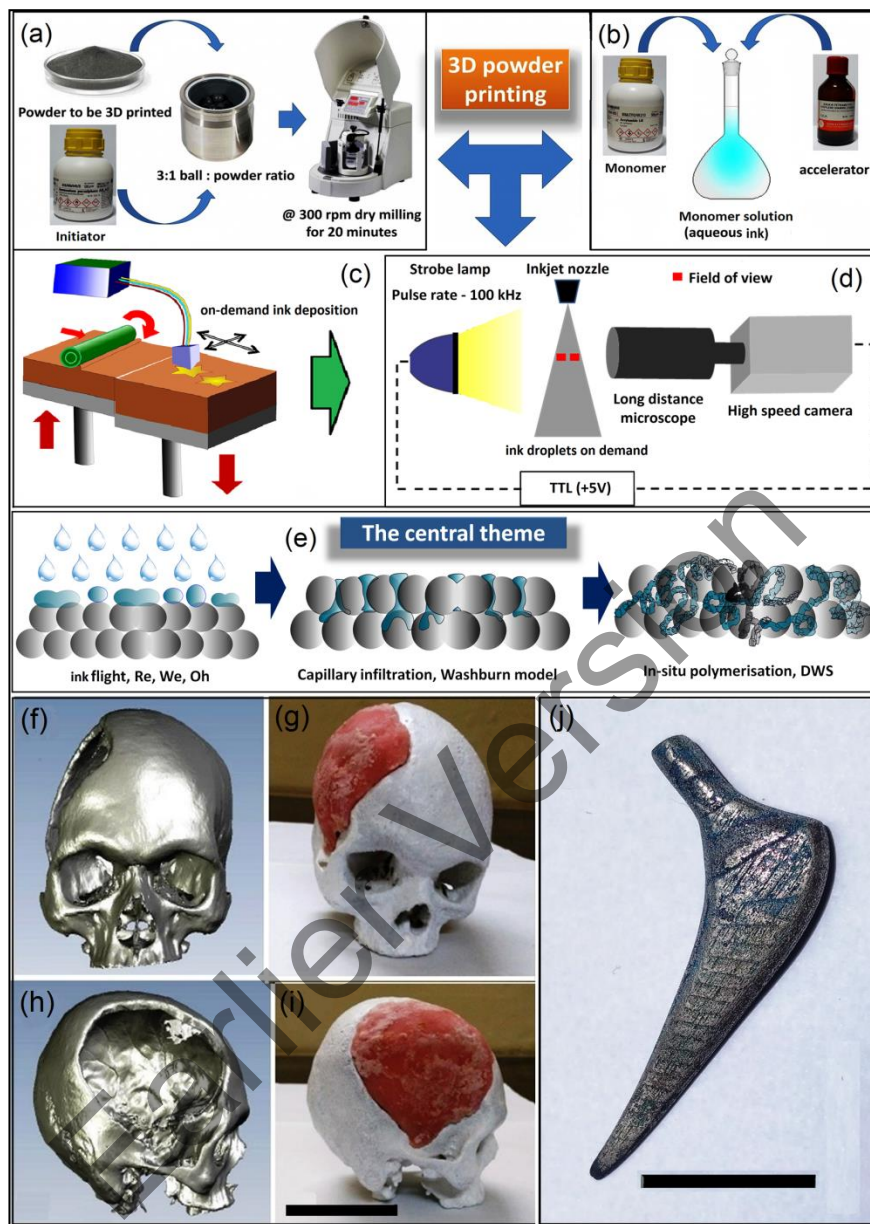


Fig. 1: Multidisciplinary experimental and theoretical approaches to study the process physics and dynamics of 3D inkjet powder printing, and its demonstrated capability to manufacture clinical models of patient-specific decompressive craniectomy and biomedical device prototype. (a) Modification of printable powder with initiator; (b) formulation of the ink (aqueous monomer solution added with accelerator); (c) 3D printing process; (d) *in-situ* shadowgraphy to capture dynamics of the as-ejected ink droplets; (e) holistic theme of the study probing several stages involved in 3D inkjet powder printing. (f – i) 50% scaled down clinical model of defective skull vault and the patient specific bone cement based cranioplast, (j) 50% scaled down printed-sintered Ti-6Al-4V human femoral stem. Scale bars, 10 cm (f – i), 16 mm (j).

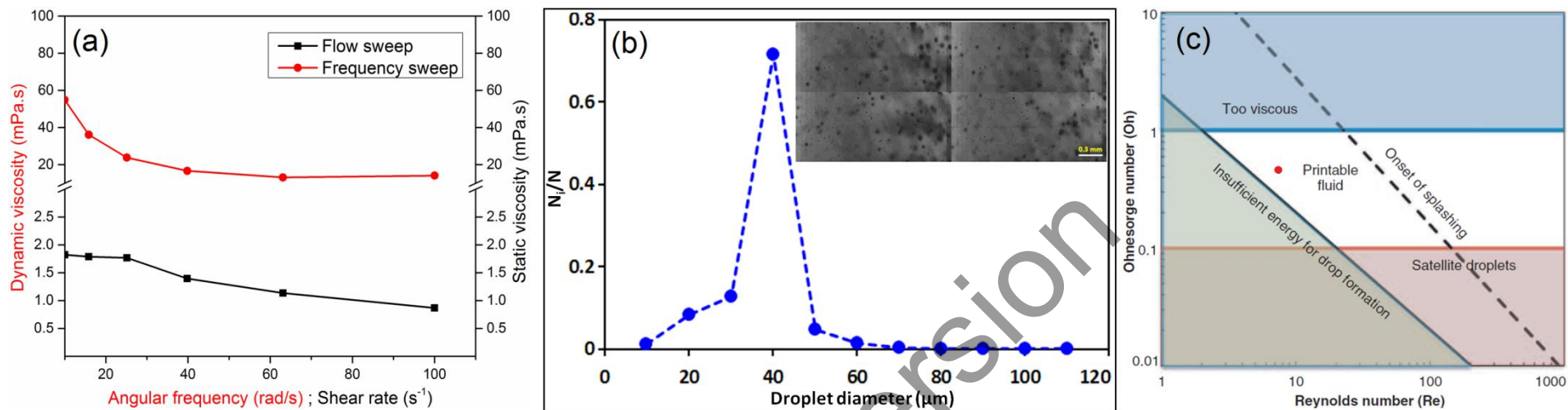


Fig. 2: Physical properties of the ink play an important role in droplet flight and inkjet printability of biomaterials. Ink viscosity from cone-plate rheometer, droplet diameter and velocity from stroboscopic shadowgraphy module, altogether are used to determine the dimensionless number of fluid physics, governing the inkjet printability. (a) Static (flow sweep) and dynamic (frequency sweep) viscosities of the ink depict the Newtonian nature and laminar flow characteristics; (b) normalised distribution of ink droplet diameters ejected from the printhead during 3D inkjet printing. N_i is the number of droplets of a particular diameter and N is the total number of droplets counted. In the inset, the appearances of the time frozen droplets are shown. Inset scale bar: 0.3 mm; (c) the acrylic ink accommodates itself (red dot) in terms of the dimensionless numbers in the 'printable fluid' region ($Re \sim 7.5$ and $Oh \sim 0.34$). Permission granted from John Wiley and Sons for use in this publication.

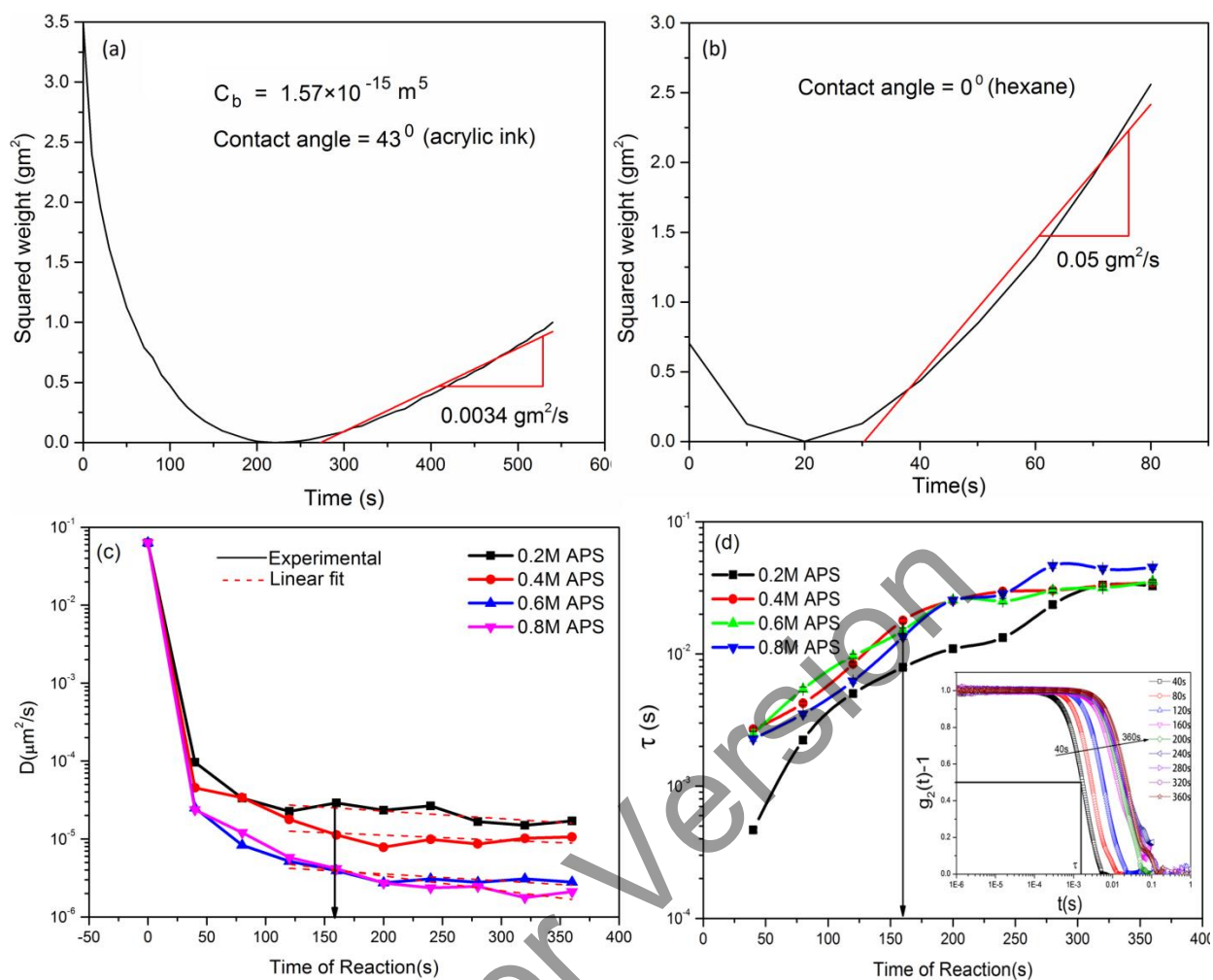


Fig. 3: The kinetics of dynamic wetting behaviour of powders and *in-situ* polymerisation behaviour involving ink-powder interactions are the major physico-chemical mechanisms driving printability in 3D inkjet based manufacturing of materials. Washburn capillary rise model is adapted to understand dynamic wetting of powder by ink during 3D inkjet printing. Squared weight versus time plot for (a) ink and (b) reference liquid (hexane) to find out the slope to fit in **equation 9**. The initial fall is due to buoyancy, during dipping the perforated end of the powder loaded shell in the corresponding liquids; Particle tracing based DWS provides insight into the *in situ* polymerization kinetics involved in 3D powder printing. (c) Plot of diffusion coefficient versus progress of reaction showing the initial falling of diffusion coefficient of the tracer particles denotes the gradual rise of viscosity of the polymerizing media with time and hindrance towards random walk; (d) plot of the half life time of decay for the photons in the media with respect to reaction time. The decay in autocorrelation function jumped to higher time after 160s of reaction, signifying the formation of macromolecular chains being able to interact with the laser photons before decaying (inset, d).

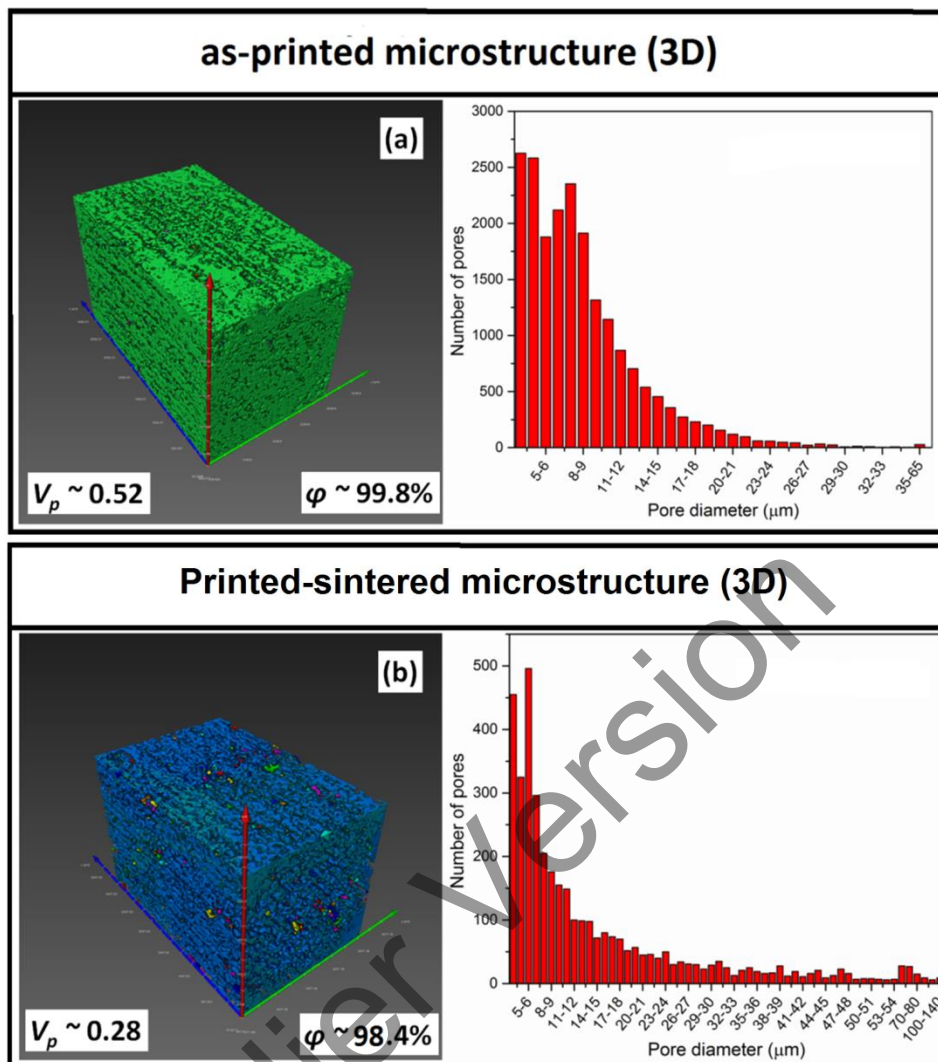


Fig. 4: Micro-computed tomography provides quantitative and qualitative analysis of 3D microstructure. Porosity analysis and the pore size distribution of the (a) as-printed and (b) sintered Ti-6Al-4V. It is evident that, pore volume fractions (V_p), pore numbers and pore interconnectivity (ϕ) reduces in sintered specimens at the expense of increment in the number average pore diameter (D_n).

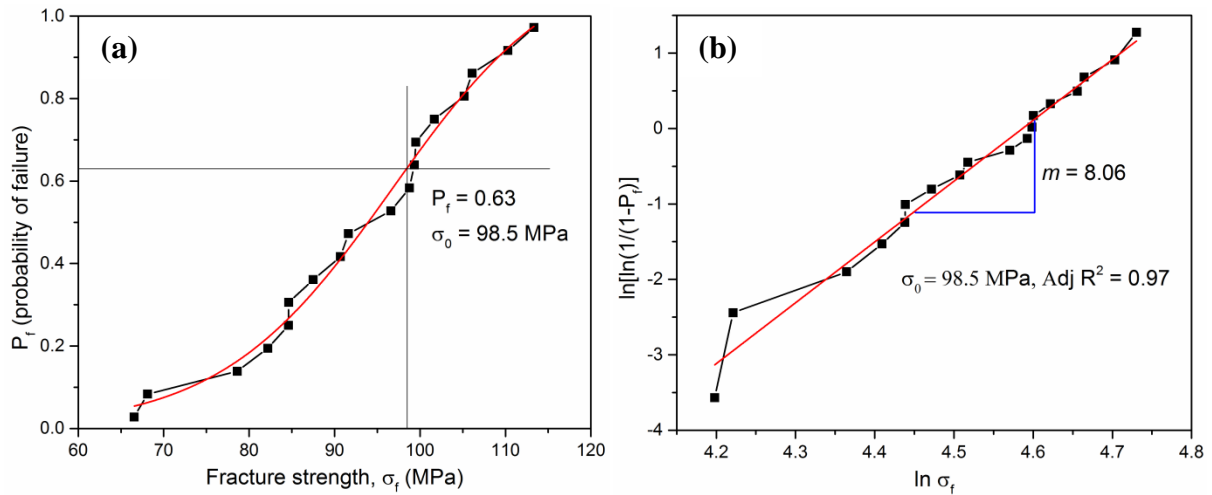


Fig. 5: Weakest link fracture statistics-based analysis of the flexural strength data using Weibull theory allows to assess the strength reliability of 3D inkjet printed and sintered Ti-6Al-4V. Sigmoid distribution of failure probability versus fracture strength (flexural). The scaling parameter assumes the value of 98.5 MPa with failure probability of 0.63 (a). Weibull probability distribution with respect to fracture strength reveals the Weibull modulus (m) value of 8.06. The adj R^2 value of 0.97 from the simple linear regression analysis exhibits the robustness of fitting strength data with Weibull theory (b).

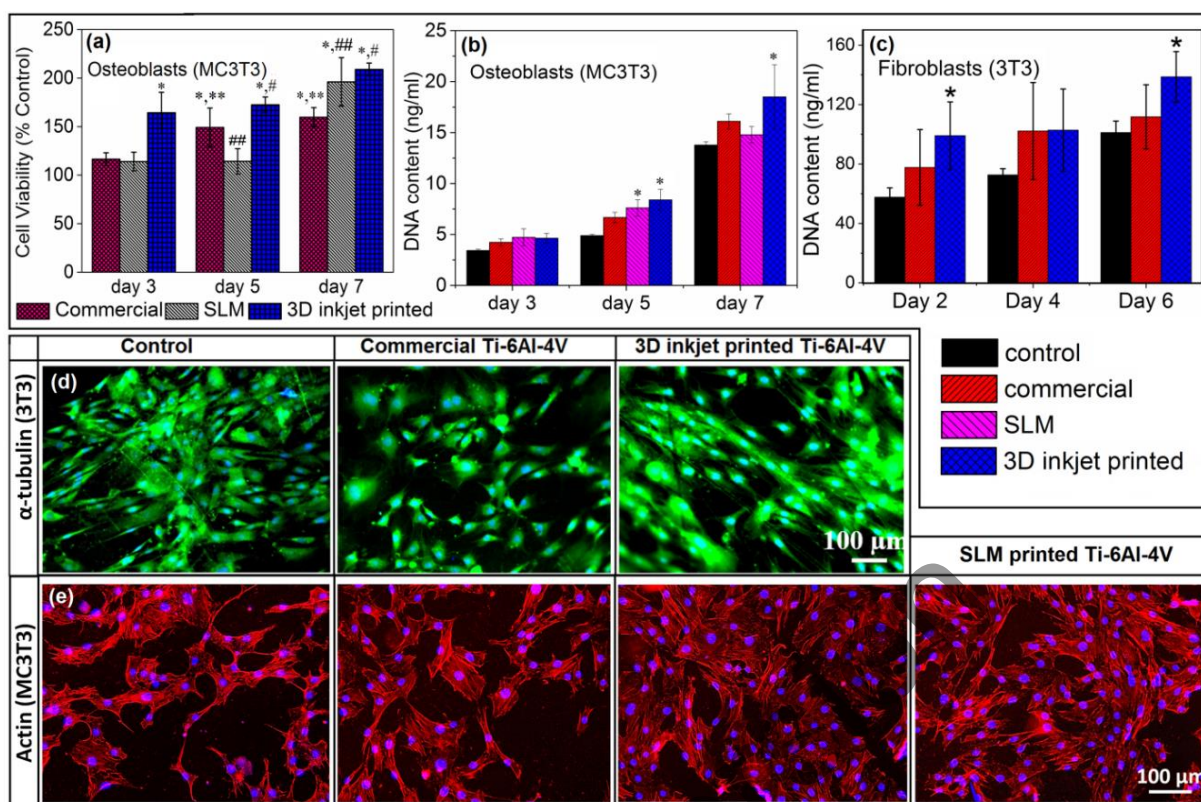


Fig. 6: Quantitative estimation of the viability (osteoblasts), proliferation induced dynamic increment in DNA content using picogreen assay (osteoblasts and fibroblasts) and qualitative representations of cytoskeletal spreading on microporous 3D inkjet printed, commercial and SLM non-porous Ti-6Al-4V substrates. (a) Consistently higher viability of osteoblasts on 3DIJPP Ti-6Al-4V compared to control in each time point. Symbol (*) denotes the significant difference with control at each time point. The viabilities on all substrates at day 5 and day 7 are significantly higher than day 3. Symbols (#, ## and **) denote the significant difference in viabilities at day 5 and day 7 in comparison with day 3 for 3DIJPP, SLM and commercial Ti-6Al-4V, respectively; (b) MC3T3 pre-osteoblast proliferation on 3DIJPP Ti-6Al-4V is significantly higher than control at both day 5 and day 7 while the same on SLM Ti-6Al-4V is significantly higher than control at day 5 and became insignificant at day 7; (c) proliferation of fibroblasts (3T3) on 3DIJPP Ti-6Al-4V is significantly higher than control on day 2 and day 6 while proliferation on the commercial Ti-6Al-4V remained consistently insignificant with control at each time point; (d) Alexafluor488 tagged microtubules (day 6) exhibit the enhanced extent of fibroblasts spreading on the inkjet printed Ti-6Al-4V, which appears to be quite similar to those on control. The spreading on commercial Ti-6Al-4V does not appear to be as efficient; (e) Rhodamine-phalloidin based immunostaining of actin filaments of osteoblasts (day 7) exhibits nearly isotropic polygonal spreading on

3DIJPP and SLM Ti-6Al-4V was observed which were not evidenced in the TCPS control and commercial Ti-6Al-4V. All the statistically significant differences in this manuscript is denoted by the cut-off value of $p < 0.05$.

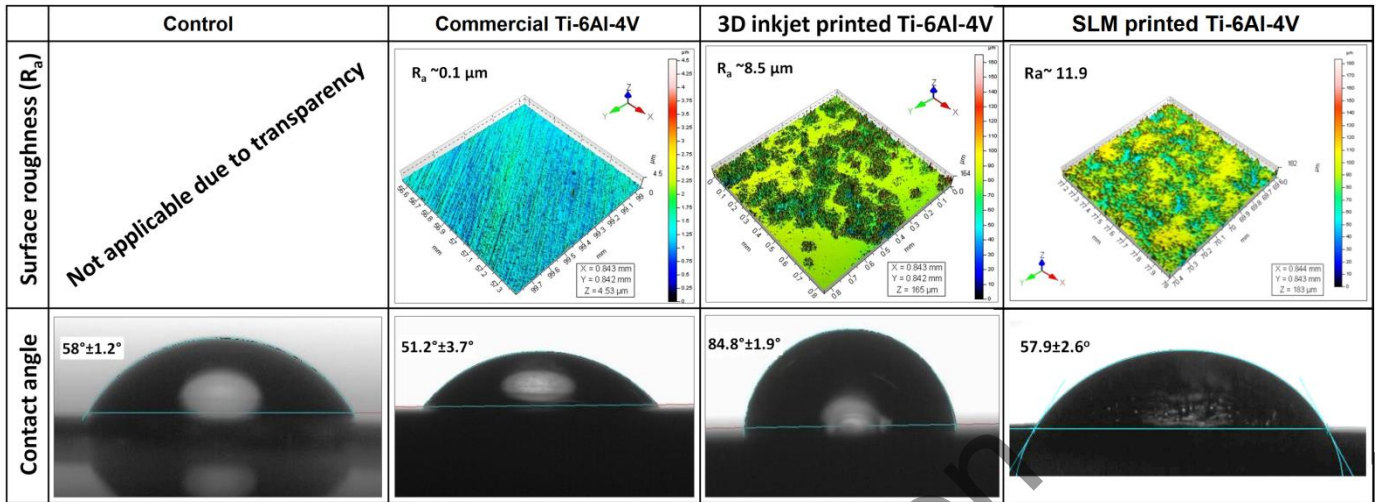


Fig. 7: Surface roughness and wettability influence cell-biomaterial interaction. Non-contact optical profilometry analysis of surface topography and contact angle, measured using sessile-drop method. Surface wettability controls protein absorption and subsequent cell adherence. 3D inkjet printed Ti-6Al-4V surface exhibits higher average roughness ($R_a \sim 8.5 \mu\text{m}$) due to the presence of micro-porosities (rough islands), leading to higher contact angle. SLM Ti-6Al-4V has higher average surface roughness than 3DIJPP due to absence of any smooth metallic matrix among the porosity islands. Owing to more homogeneously distributed rough surface, it leads to have lower contact angle for the SLM than the 3DIJPP TI-6Al-4V.

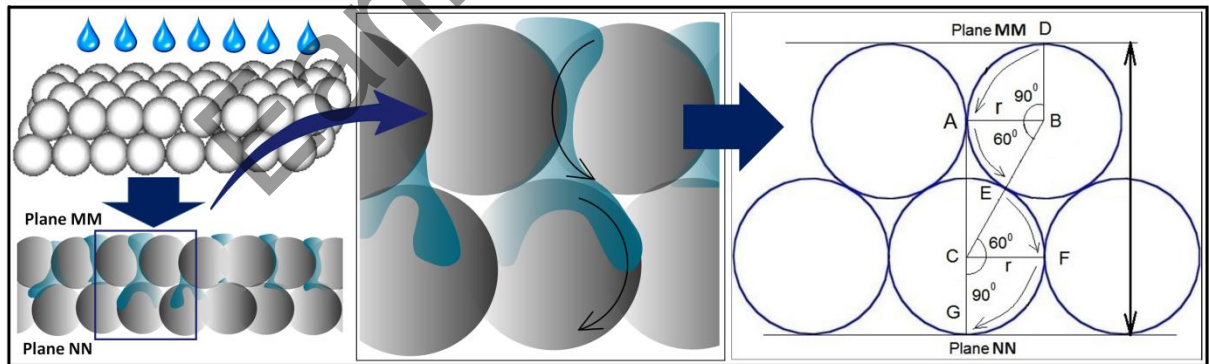


Fig. 8: Carman's model validated in analyzing geometric configuration parameters of the powder packing arrangement to establish theoretical foundation of 3D inkjet powder printing. During infiltration through the stacked particles, the liquid droplets travel a tortuous path while moving down over the spherical surfaces of particles layer-by-layer. The ratio between the tortuous path and the vertical distance for a porous layer can be calculated to be $\sqrt{2}$. The model is valid in the assumption of closely packed spherical particles.

List of Tables:

Table 1: Shadowgraphy based *in situ* measurements of the ink droplet diameter (D) and velocity (v) of traveling droplets during drop-on-demand inkjet printing. The dimensionless numbers were calculated using the diameter, velocity of droplets and the values of surface tension and viscosity.

D_{\min} (μm)	D_{\max} (μm)	D_{av} (D_{10} , μm)	v_{\min} (m/s)	v_{\max} (m/s)
8 - 15	70-77	42	0.1 - 0.5	2.5
Fluid parameters	Weber number (We)	Reynolds number (Re)	Ohnesorge number (Oh)	Dynamic viscosity (mPa.s)
Acrylic ink	6.44	7.5	0.34	~16

Table 2: Quantitative 3D microstructure analysis using micro-computed tomography to determine porosity parameters in as-printed and sintered Ti-6Al-4V.

Porous specimens	Pore volume fraction (V_p)	Pore interconnectivity (ϕ , %)	Number average pore diameter (D_n , μm)
As-printed Ti-6Al-4V	0.52	99.8	8.9
As-sintered Ti-6Al-4V	0.28	98.4	12.5

Table 3: Summary of achieved mechanical properties of the as-sintered and polished Ti-6Al-4V specimens. For comparison, the Weibull modulus of bovine cortical bone measured under compression together with other properties of cortical bone are summarized from literature [44-53].

	Ultimate compressive strength (MPa)	Compressive modulus, (GPa)	Vicker's hardness (GPa)	Average flexural strength (MPa)	Weibull modulus (m)	Scaling strength (σ_0 , MPa)
Inkjet printed Ti-6Al-4V	222.6 ± 32.2	4.1 ± 0.3	6.2 ± 0.8	92.5	8.1 (flexural)	98.5
Cortical bone	122 - 142	2-12	0.4 – 0.7	50-150	7.2 (compressive, bovine cortical)	--

Table 4: Comparative mechanical properties achieved in different additive manufacturing approaches for processing Ti and Ti-6Al-4V

3D inkjet powder printing	Reported binders for 3D powder printing of Ti and Ti6Al4V	Sintering temperature (°C)	Compression Strength (MPa)	Compressive modulus (GPa)
	Deionised water as binder for Ti premixed with PVA powder[38]	1300	107.2	0.86
	Deionised water as binder fir Ti premixed with PVA powder[39]	1370	-	2.5
	Aqueous Maltodextrin solution as binder for Ti-6Al-4V powder[21]	1400	200	4.0
	<i>in situ</i> polymerisable acrylic binder for metal printing	1400	222.6	4.1
High energy fusion/melting of powder bed for non-porous architectures	Powder bed fusion methods	Laser/Electron beam energy	Tensile strength (MPa)	Elastic modulus (GPa)
	EBM[40]	--	775	93
	SLM[41]	120-200W	1095	110
	EBM[42]	100 kW/cm ²	1150	--
	SLM[43]	--	1219-1274	--

Supplementary section:

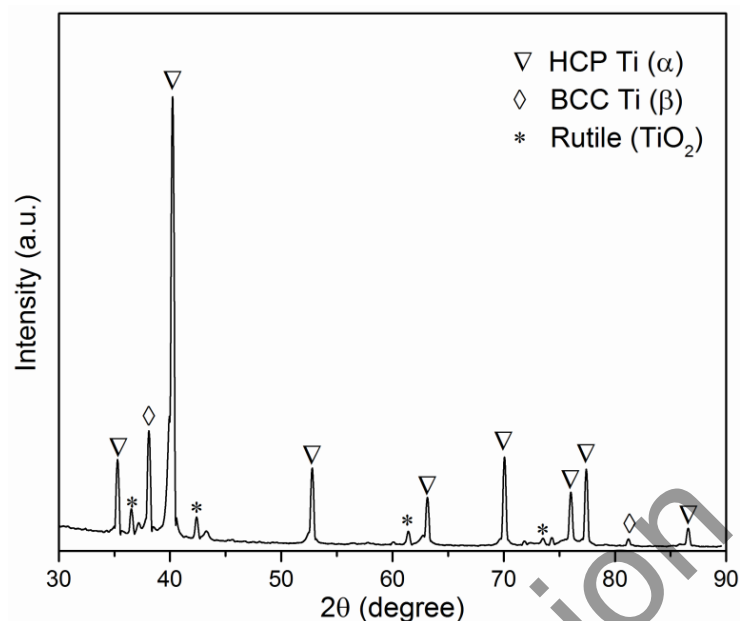


Fig. S1: X-ray diffraction pattern of sintered Ti-6Al-4V showing the predominance of the HCP α -phase in the microstructure. Some extent of rutile formation was also evident which was probably due to exposure of the powder in the air during printing and utilization of the aqueous binder.

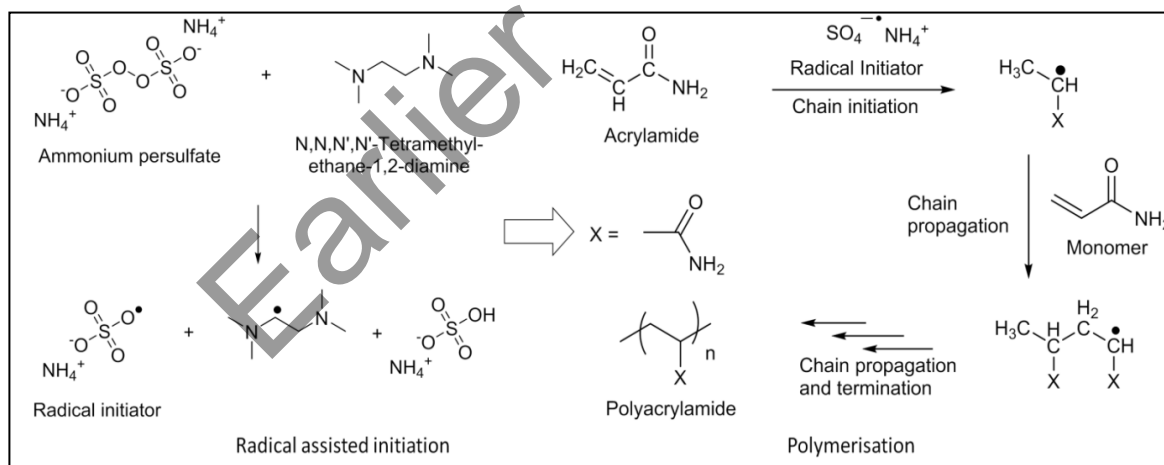


Fig. S2: *in situ* polymerization plays the key role in powder-ink interaction. Schematic of the adapted polymerisation reaction of acrylamide added with TEMED in the presence of APS pre-mixed with the powder to be printed. TEMED stabilizes the nascent free radicals generated from the dissociation of persulfate bond of APS and assists to attack the α -center of acrylamide. The reactive free radical site of the monomer attacks double bonds of other monomers present in the solution and add them subsequently to the backbone to increase the chain length.

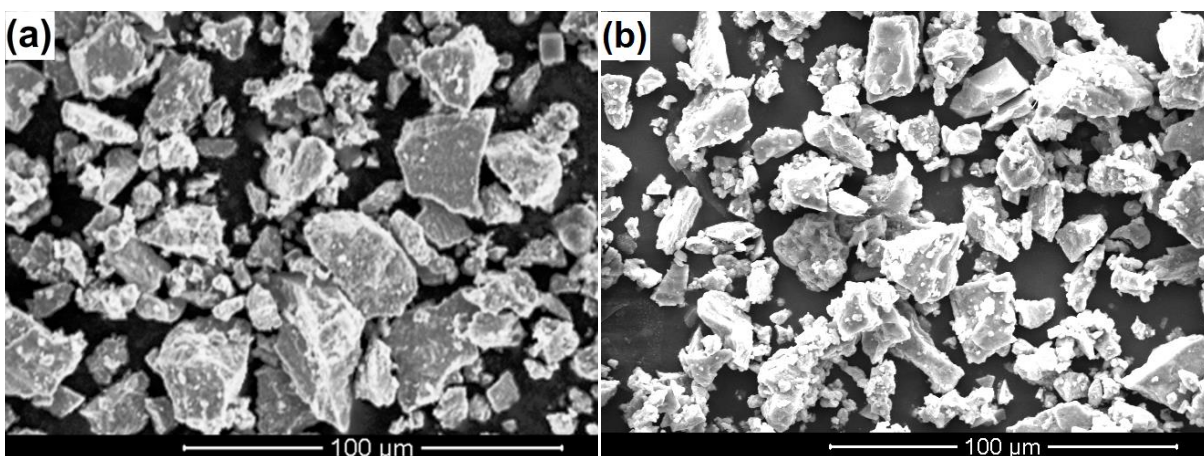


Fig. S3: Powder particle diameter influences the ink infiltration time. Morphology of the as received (a) and APS modified Ti-6Al-4V powders by ball milling (b).

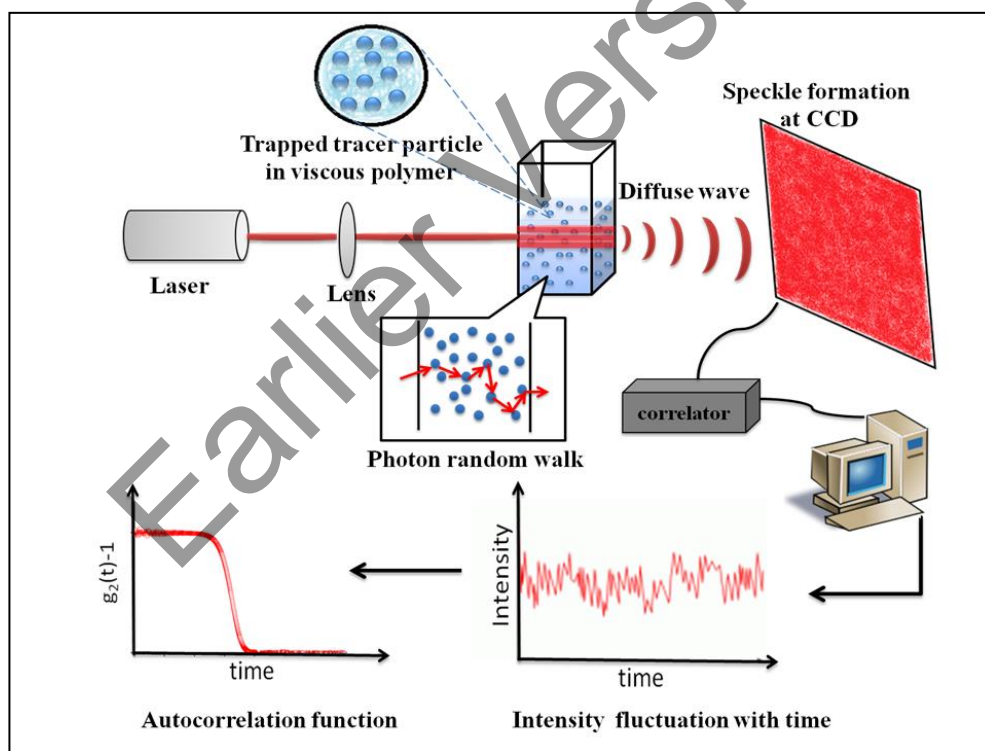


Fig. S4: Schematic representation of working principle of diffusing wave spectroscopy. The delayed decay in autocorrelation function attributes to the more intermediate interactions with the macromolecules interfering in the optical path.

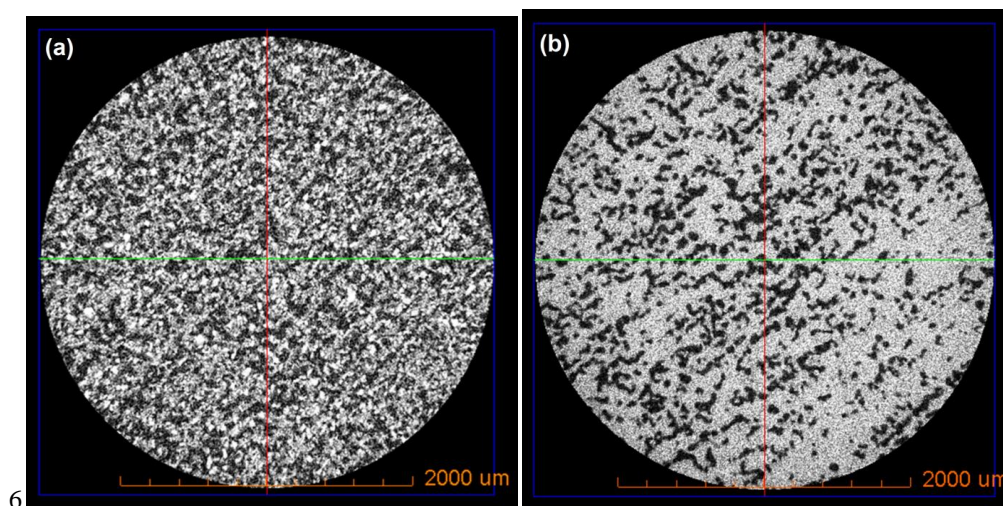


Fig. S5: 2D porous surface morphologies perceived from the orthoslices of as-printed Ti-6Al-4V (a) and as-sintered Ti-6Al-4V (b), obtained from high resolution micro-CT scan. The decrease in pore number, interconnectivity and increment in pore sizes are clearly visible after sintering.

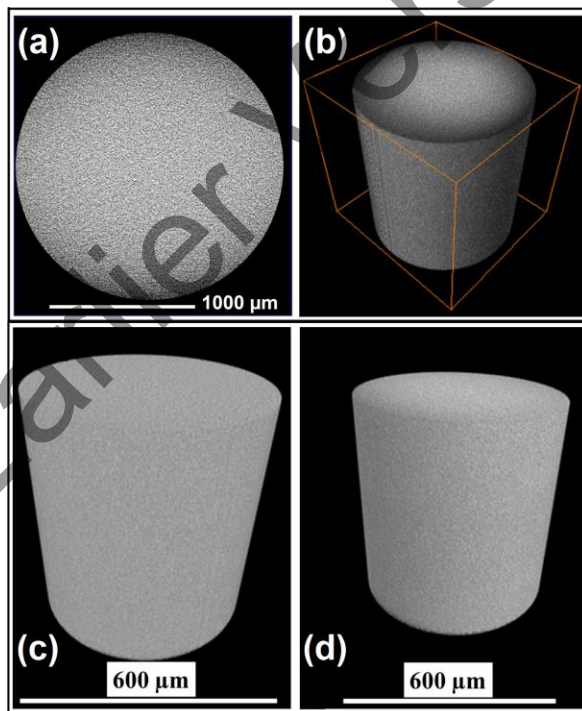


Fig. S6: The 2D orthoslice (a) and 3D volume rendered microstructure (b) from micro-computed tomogram of the non-porous metallurgically processed (commercial) Ti-6Al-4V. 3D volume rendered non-porous microstructure of the SLM Ti-6Al-4V referred in this study[38] (permission granted by Elsevier for reproducing in this article); (c) horizontally printed and (d) vertically printed samples

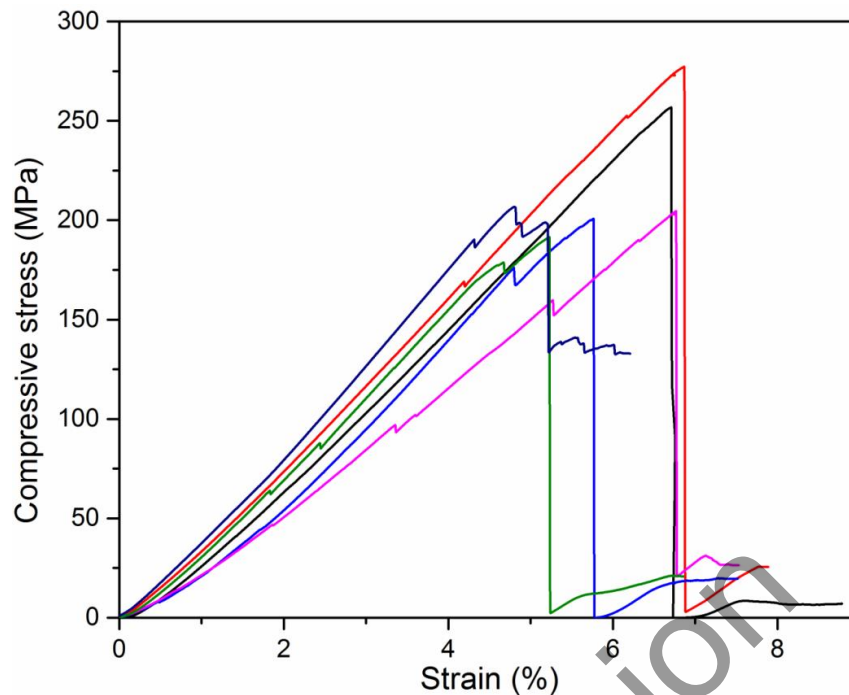


Fig. S7: Representative stress-strain plots of printed-sintered microporous Ti-6Al-4V cylinders demonstrate brittle nature of failure. The kinks appear due to progressive failure of the porous layers.

➤ **Fibronectin assay for immunocytochemistry of 3T3 cells**

3T3 cells grown on the surfaces of inkjet printed microporous Ti-6Al-4V and commercially available Ti-6Al-4V along with the controls were fixed by using 4% paraformaldehyde (PFA, SDFCL) solution. Subsequently, the cells were permeabilised with 0.1% of triton X and blocked with 1% Bovine Serum Albumin (BSA) to prevent the unwanted non-specific binding of the dye. Primary antibodies of fibronectin (Abcam, ab2413) were added at dilution of 1:200 for 1 h. Secondary antibody of goat with fluorophore tagging [AF488 (A 11029)] was added at the 1:650 dilution and kept for 1 hr. The cells were observed under fluorescence microscope (Nikon LV 100D, Japan).

The modulated cytocompatibility of the 3D printed Ti-6Al-4V corroborates well with the fibronectin protein expression. The extent of focal adhesion complexes on a biomaterial substrate, in turn, mediates the cell attachment, and further triggers cell spreading and

proliferation. From **Fig. S8**, it is observed that, the expression of the interactive fibronectin proteins (green spots in group) are higher in the case of 3D inkjet printed Ti-6Al-4V, when compared to control and the commercial Ti-6Al-4V.

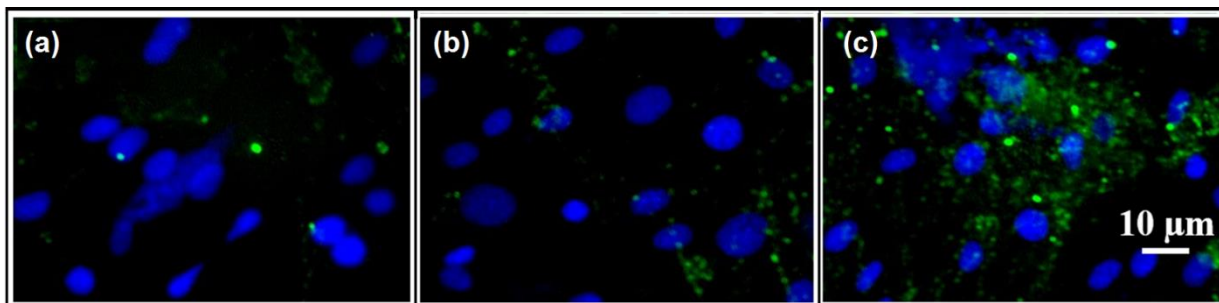


Fig. S8: Enhanced fibroblast adhesion was evidenced in the fibronectin protein expression, where extensive focal adhesion complex linking the integrin proteins was found to be present on inkjet printed Ti-6Al-4V (c), indicating good cell-material adhesion. The green spots essentially express the fibronectin protein around cell-biomaterial interface. The fluorescent green spots in (a) and (b) represent the fibronectin expression of TCPS control and commercial Ti-6Al-4V respectively.

➤ Calcium activity of 3T3 cells on commercial and 3DIJPP Ti-6Al-4V

Fluo-4 AM is a non-toxic calcium detecting fluorescent probe. The loading of the dye to live cells is essential for detecting calcium activities, which indicate both survivability and apoptosis, depending on the ion concentration. The cultured fibroblasts were loaded with Fluo-4 AM (Invitrogen) using the final concentration of 2 μM along with 0.1% Pluronic F-127 in 1 mL of HEPES buffer. The later was used as the loading detergent. The samples were incubated at 37 $^{\circ}\text{C}$ for 30 min and the dye was allowed to be deesterified by the cellular activities which enhance the intensity of the emitted fluorescence. The dye loaded cells with tagged intracellular-calcium were imaged in a fluorescence microscope using excitation wavelength of 494 nm and emission at 516 nm.

Calcium (Ca^{2+}) ions take part in cellular signaling in terms of triggering various allosteric regulatory influences on various enzymes and proteins. As shown in **Fig. S9**, the calcium activities after 6 days of culture for the fibroblasts on the 3D inkjet printed Ti-6Al-4V specimens exhibited almost similar behavior like the TCPS control and commercial Ti-6Al-4V. This is also consistent with the Ca-intensity plots, measured on the basis of fluorescence intensity variation.

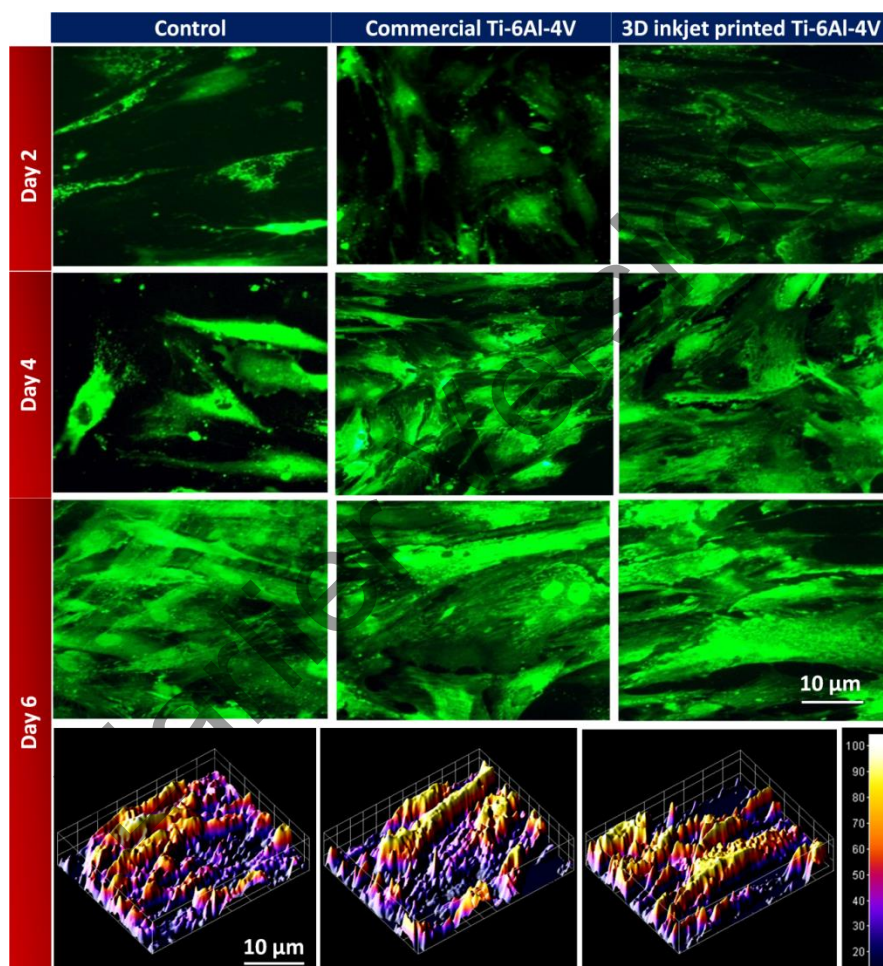


Fig. S9: Fluo-4 AM staining of cultured cells provide signatures of intracellular calcium activity. Representative fluorescence microscopic images of Fluo-4 tagged 3T3 murine fibroblasts on the 3D inkjet printed Ti-6Al-4V and the commercial Ti-6Al-4V at different time points in culture, exhibiting metabolically healthy cellular activities. The dynamic increments in the Ca^{2+} expressions are similar on all the biomaterial substrates. The color scale depicts the entire range of the Ca^{2+} expression, evolving from the blue (zero expression) towards white (maximum expression).

Data availability

The authors are always open to share the data anytime if requested by the peer reviewers or the editorial office.

References:

- [1] Hollister SJ. Porous scaffold design for tissue engineering. *Nat Mater* 2005;4:518-24.
- [2] Murphy SV, Atala A. 3D bioprinting of tissues and organs. *Nat Biotech* 2014;32:773-85.
- [3] Derby B. Printing and Prototyping of Tissues and Scaffolds. *Science* 2012;338:921.
- [4] Hinton TJ, Jallerat Q, Palchesko RN, Park JH, Grodzicki MS, Shue H-J, et al. Three-dimensional printing of complex biological structures by freeform reversible embedding of suspended hydrogels. *Science Advances* 2015;1.
- [5] Truby RL, Lewis JA. Printing soft matter in three dimensions. *Nature* 2016;540:371-8.
- [6] Giannopoulos AA, Mitsouras D, Yoo S-J, Liu PP, Chatzizisis YS, Rybicki FJ. Applications of 3D printing in cardiovascular diseases. *Nat Rev Cardiol* 2016;13:701-18.
- [7] Meininger S, Mandal S, Kumar A, Groll J, Basu B, Gbureck U. Strength reliability and in vitro degradation of three-dimensional powder printed strontium-substituted magnesium phosphate scaffolds. *Acta Biomaterialia* 2016;31:401-11.
- [8] Basu B. *Biomaterials for Musculoskeletal Regeneration: Concepts*: Springer Nature; 2016.
- [9] Basu B, Ghosh S. *Biomaterials for Musculoskeletal Regeneration: Applications*: Springer Nature; 2016.
- [10] Basu B. *Biomaterials Science and Tissue Engineering: Principles and Methods* (Cambridge University Press, 2017).
- [11] Barui S, Chatterjee S, Mandal S, Kumar A, Basu B. Microstructure and compression properties of 3D powder printed Ti-6Al-4V scaffolds with designed porosity: Experimental and computational analysis. *Materials Science and Engineering: C* 2017;70:812-23.
- [12] Habibovic P, Gbureck U, Doillon CJ, Bassett DC, van Blitterswijk CA, Barralet JE. Osteoconduction and osteoinduction of low-temperature 3D printed bioceramic implants. *Biomaterials* 2008;29:944-53.
- [13] Gbureck U, Hölzel T, Doillon CJ, Müller FA, Barralet JE. Direct Printing of Bioceramic Implants with Spatially Localized Angiogenic Factors. *Advanced Materials* 2007;19:795-800.
- [14] Kumar A, Mandal S, Barui S, Vasireddi R, Gbureck U, Gelinsky M, et al. Low temperature additive manufacturing of three dimensional scaffolds for bone-tissue engineering applications: Processing related challenges and property assessment. *Materials Science and Engineering: R: Reports* 2016;103:1-39.
- [15] Galet L, Patry S, Dodds J. Determination of the wettability of powders by the Washburn capillary rise method with bed preparation by a centrifugal packing technique. *Journal of Colloid and Interface Science* 2010;346:470-5.
- [16] Kirdponpattara S, Phisalaphong M, Newby B-mZ. Applicability of Washburn capillary rise for determining contact angles of powders/porous materials. *Journal of Colloid and Interface Science* 2013;397:169-76.
- [17] Kiesvaara J, Yliruusi J. The use of the Washburn method in determining the contact angles of lactose powder. *International Journal of Pharmaceutics* 1993;92:81-8.
- [18] Weitz DA, Zhu JX, Durian DJ, Gang H, Pine DJ. Diffusing-Wave Spectroscopy - the Technique and Some Applications. *Physica Scripta* 1993;T49b:610-21.
- [19] Mason TG, Weitz D. Optical measurements of frequency-dependent linear viscoelastic moduli of complex fluids. *Physical review letters* 1995;74:1250.

- [20] Breugem AJ, Bouchama F, Koper GJM. Diffusing wave spectroscopy: A novel rheological method for drying paint films. *Surface Coatings International Part B: Coatings Transactions* 2005;88:135-8.
- [21] Narita T, Knaebel A, Munch J-P, Candau SJ. Microrheology of Poly(vinyl alcohol) Aqueous Solutions and Chemically Cross-Linked Gels. *Macromolecules* 2001;34:8224-31.
- [22] Guo S, Liu R, Jiang X, Zhang H, Zhang D, Wang J, et al. Statistical Analysis on the Mechanical Properties of Magnesium Alloys. *Materials* 2017;10:1271.
- [23] Quinn JB, Quinn GD. A practical and systematic review of Weibull statistics for reporting strengths of dental materials. *Dental Materials* 2010;26:135-47.
- [24] Hong K, Zhang H, Mays JW, Visser AE, Brazel CS, Holbrey JD, et al. Conventional free radical polymerization in room temperature ionic liquids: a green approach to commodity polymers with practical advantages. *Chemical Communications* 2002:1368-9.
- [25] Saunders RE, Derby B. Inkjet printing biomaterials for tissue engineering: bioprinting. *International Materials Reviews* 2014;59:430-48.
- [26] Kovalchuk NM, Nowak E, Simmons MJH. Kinetics of liquid bridges and formation of satellite droplets: Difference between micellar and bi-layer forming solutions. *Colloids and Surfaces A: Physicochemical and Engineering Aspects* 2017;521:193-203.
- [27] Barui S, Mandal S, Basu B. Thermal inkjet 3D powder printing of metals and alloys: current status and challenges. *Current Opinion in Biomedical Engineering* 2017.
- [28] Martin GD, Hutchings IM. *Fundamentals of Inkjet Technology. Inkjet Technology for Digital Fabrication: John Wiley & Sons, Ltd; 2012. p. 21-44.*
- [29] Reis N, Derby B. Ink Jet Deposition of Ceramic Suspensions: Modeling and Experiments of Droplet Formation. *MRS Proceedings* 2011;625.
- [30] Bell JM, Cameron FK. The Flow of Liquids through Capillary Spaces. *The Journal of Physical Chemistry* 1905;10:658-74.
- [31] Washburn EW. The Dynamics of Capillary Flow. *Physical Review* 1921;17:273-83.
- [32] Carman PC. *Flow of gases through porous media.* New York: Academic Press; 1956.
- [33] Cicuta P, Donald AM. Microrheology: a review of the method and applications. *Soft Matter* 2007;3:1449-55.
- [34] Tsuji M, Ueda T, Sawaki K, Kawaguchi M, Sakurai K. Biocompatibility of a titanium dioxide-coating method for denture base acrylic resin. *Gerodontology* 2016;33:539-44.
- [35] Abou Neel EA, Knowles JC. Physical and biocompatibility studies of novel titanium dioxide doped phosphate-based glasses for bone tissue engineering applications. *Journal of Materials Science: Materials in Medicine* 2008;19:377-86.
- [36] Sabetrasekh R, Tiainen H, Lyngstadaas SP, Reseland J, Haugen H. A Novel Ultra-porous Titanium Dioxide Ceramic with Excellent Biocompatibility. *Journal of Biomaterials Applications* 2011;25:559-80.
- [37] Miller JS, Stevens KR, Yang MT, Baker BM, Nguyen D-HT, Cohen DM, et al. Rapid casting of patterned vascular networks for perfusable engineered three-dimensional tissues. *Nat Mater* 2012;11:768-74.
- [38] Sabban R, Bahl S, Chatterjee K, Suwas S. Globularization using heat treatment in additively manufactured Ti-6Al-4V for high strength and toughness. *Acta Materialia* 2019;162:239-54.
- [39] Gagg G, Ghassemieh E, Wiria FE. Effects of sintering temperature on morphology and mechanical characteristics of 3D printed porous titanium used as dental implant. *Materials Science and Engineering: C* 2013;33:3858-64.
- [40] El-Hajje A, Kolos E, Wang J, Maleksaedi S, He Z, Wiria F, et al. Physical and mechanical characterisation of 3D-printed porous titanium for biomedical applications. *J Mater Sci: Mater Med* 2014;25:2471-80.
- [41] Koike M, Martinez K, Guo L, Chahine G, Kovacevic R, Okabe T. Evaluation of titanium alloy fabricated using electron beam melting system for dental applications. *Journal of Materials Processing Technology* 2011;211:1400-8.

- [42] Wissenbach K, Höges S, Robotti P, Molinari A, Facchini L, Magalini E. Ductility of a Ti-6Al-4V alloy produced by selective laser melting of prealloyed powders. *Rapid Prototyping Journal* 2010;16:450-9.
- [43] Murr LE, Esquivel EV, Quinones SA, Gaytan SM, Lopez MI, Martinez EY, et al. Microstructures and mechanical properties of electron beam-rapid manufactured Ti-6Al-4V biomedical prototypes compared to wrought Ti-6Al-4V. *Materials Characterization* 2009;60:96-105.
- [44] Havaladar R, Pilli S, Putti B. Insights into the effects of tensile and compressive loadings on human femur bone. *Advanced Biomedical Research* 2014;3:101-.
- [45] Bayraktar HH, Morgan EF, Niebur GL, Morris GE, Wong EK, Keaveny TM. Comparison of the elastic and yield properties of human femoral trabecular and cortical bone tissue. *Journal of Biomechanics* 2004;37:27-35.
- [46] Reilly DT, Burstein AH. The elastic and ultimate properties of compact bone tissue. *Journal of Biomechanics* 1975;8:393-405.
- [47] Zwierzak I, Baleani M, Viceconti M. Microindentation on cortical human bone: Effects of tissue condition and indentation location on hardness values. *Proceedings of the Institution of Mechanical Engineers, Part H: Journal of Engineering in Medicine* 2009;223:913-8.
- [48] Rho J-Y, Tsui TY, Pharr GM. Elastic properties of human cortical and trabecular lamellar bone measured by nanoindentation. *Biomaterials* 1997;18:1325-30.
- [49] Zioupos P, Currey JD. Changes in the Stiffness, Strength, and Toughness of Human Cortical Bone With Age. *Bone* 1998;22:57-66.
- [50] Li S, Demirci E, Silberschmidt VV. Variability and anisotropy of mechanical behavior of cortical bone in tension and compression. *Journal of the Mechanical Behavior of Biomedical Materials* 2013;21:109-20.
- [51] Keller TS, Mao Z, Spengler DM. Young's modulus, bending strength, and tissue physical properties of human compact bone. *Journal of Orthopaedic Research* 1990;8:592-603.
- [52] Ebacher V, Tang C, McKay H, Oxland TR, Guy P, Wang R. Strain redistribution and cracking behavior of human bone during bending. *Bone* 2007;40:1265-75.
- [53] Roohani-Esfahani S-I, Newman P, Zreiqat H. Design and Fabrication of 3D printed Scaffolds with a Mechanical Strength Comparable to Cortical Bone to Repair Large Bone Defects. 2016;6:19468.
- [54] Weibull W. A Statistical Distribution Function of Wide Applicability. *Journal of Applied Mechanics* 1952;18:293-7.
- [55] Calvo M. Application of the Weibull statistics to the characterization of metallic glass ribbons. *Journal of Materials Science* 1989;24:1801-8.
- [56] Tiryakioğlu M, Hudak D. Guidelines for Two-Parameter Weibull Analysis for Flaw-Containing Materials. *Metallurgical and Materials Transactions B* 2011;42:1130-5.
- [57] Babuska V, Dobra J, Kulda V, Kripnerova M, Moztarzadeh A, Bolek L, et al. Comparison of Fibroblast and Osteoblast Response to Cultivation on Titanium Implants with Different Grain Sizes. *Journal of Nanomaterials* 2015;2015:9.
- [58] Bordji K, Jouzeau JY, Mainard D, Payan E, Netter P, Rie KT, et al. Cytocompatibility of Ti-6Al-4V and Ti-5Al-2.5Fe alloys according to three surface treatments, using human fibroblasts and osteoblasts. *Biomaterials* 1996;17:929-40.
- [59] Hu X, Neoh KG, Shi Z, Kang E-T, Wang W. An In Vitro Assessment of Fibroblast and Osteoblast Response to Alendronate-Modified Titanium and the Potential for Decreasing Fibrous Encapsulation. *Tissue Engineering Part A* 2013;19:1919-30.
- [60] Yang Y, Kulangara K, Lam RTS, Dharmawan R, Leong KW. Effects of Topographical and Mechanical Property Alterations Induced by Oxygen Plasma Modification on Stem Cell Behavior. *ACS Nano* 2012;6:8591-8.
- [61] Moeendarbary E, Harris AR. Cell mechanics: principles, practices, and prospects. *Wiley Interdisciplinary Reviews: Systems Biology and Medicine* 2014;6:371-88.
- [62] Vining KH, Mooney DJ. Mechanical forces direct stem cell behaviour in development and regeneration. *Nature reviews Molecular cell biology* 2017;18:728-42.

- [63] Mitra J, Jain S, Sharma A, Basu B. Patterned growth and differentiation of neural cells on polymer derived carbon substrates with micro/nano structures in vitro. *Carbon* 2013;65:140-55.
- [64] Engler AJ, Sen S, Sweeney HL, Discher DE. Matrix Elasticity Directs Stem Cell Lineage Specification. *Cell* 2006;126:677-89.
- [65] Baker SC, Rohman G, Southgate J, Cameron NR. The relationship between the mechanical properties and cell behaviour on PLGA and PCL scaffolds for bladder tissue engineering. *Biomaterials* 2009;30:1321-8.
- [66] Jain S, Webster TJ, Sharma A, Basu B. Intracellular reactive oxidative stress, cell proliferation and apoptosis of Schwann cells on carbon nanofibrous substrates. *Biomaterials* 2013;34:4891-901.
- [67] Jones AC, Arns CH, Hutmacher DW, Milthorpe BK, Sheppard AP, Knackstedt MA. The correlation of pore morphology, interconnectivity and physical properties of 3D ceramic scaffolds with bone ingrowth. *Biomaterials* 2009;30:1440-51.
- [68] Chen Y, Frith JE, Dehghan-Manshadi A, Attar H, Kent D, Soro NDM, et al. Mechanical properties and biocompatibility of porous titanium scaffolds for bone tissue engineering. *Journal of the Mechanical Behavior of Biomedical Materials* 2017;75:169-74.
- [69] Zareidoost A, Yousefpour M, Ghaseme B, Amanzadeh A. The relationship of surface roughness and cell response of chemical surface modification of titanium. *Journal of Materials Science: Materials in Medicine* 2012;23:1479-88.
- [70] Feller L, Jadwat Y, Khammissa RAG, Meyerov R, Schechter I, Lemmer J. Cellular Responses Evoked by Different Surface Characteristics of Intraosseous Titanium Implants. *BioMed Research International* 2015;2015:8.
- [71] Jemat A, Ghazali MJ, Razali M, Otsuka Y. Surface Modifications and Their Effects on Titanium Dental Implants. *BioMed Research International* 2015;2015:11.
- [72] Gittens RA, McLachlan T, Olivares-Navarrete R, Cai Y, Berner S, Tannenbaum R, et al. The effects of combined micron-/submicron-scale surface roughness and nanoscale features on cell proliferation and differentiation. *Biomaterials* 2011;32:3395-403.
- [73] Boyan BD, Hummert TW, Dean DD, Schwartz Z. Role of material surfaces in regulating bone and cartilage cell response. *Biomaterials* 1996;17:137-46.
- [74] Kieswetter K, Schwartz Z, Hummert TW, Cochran DL, Simpson J, Dean DD, et al. Surface roughness modulates the local production of growth factors and cytokines by osteoblast-like MG-63 cells. *Journal of Biomedical Materials Research* 1996;32:55-63.
- [75] Schwartz Z, Martin JY, Dean DD, Simpson J, Cochran DL, Boyan BD. Effect of titanium surface roughness on chondrocyte proliferation, matrix production, and differentiation depends on the state of cell maturation. *Journal of Biomedical Materials Research* 1996;30:145-55.
- [76] Hallab NJ, Bundy KJ, O'Connor K, Moses RL, Jacobs JJ. Evaluation of Metallic and Polymeric Biomaterial Surface Energy and Surface Roughness Characteristics for Directed Cell Adhesion. *Tissue Engineering* 2001;7:55-71.
- [77] Trappmann B, Gautrot JE, Connelly JT, Strange DGT, Li Y, Oyen ML, et al. Extracellular-matrix tethering regulates stem-cell fate. *Nature Materials* 2012;11:642.
- [78] Mei Y, Saha K, Bogatyrev SR, Yang J, Hook AL, Kalcioğlu ZI, et al. Combinatorial development of biomaterials for clonal growth of human pluripotent stem cells. *Nature Materials* 2010;9:768.
- [79] Reilly GC, Engler AJ. Intrinsic extracellular matrix properties regulate stem cell differentiation. *Journal of Biomechanics* 2010;43:55-62.
- [80] Ross AM, Jiang Z, Bastmeyer M, Lahann J. Physical Aspects of Cell Culture Substrates: Topography, Roughness, and Elasticity. *Small* 2012;8:336-55.
- [81] Naskar S, Panda AK, Kumaran V, Mehta B, Basu B. Controlled Shear Flow Directs Osteogenesis on UHMWPE-Based Hybrid Nanobiocomposites in a Custom-Designed PMMA Microfluidic Device. *ACS Applied Bio Materials* 2018;1:414-35.
- [82] Naskar S, Kumaran V, Basu B. On The Origin of Shear Stress Induced Myogenesis Using PMMA Based Lab-on-Chip. *ACS Biomaterials Science & Engineering* 2017;3:1154-71.
- [83] Piret G, Perez M-T, Prinz CN. Substrate porosity induces phenotypic alterations in retinal cells cultured on silicon nanowires. *RSC Advances* 2014;4:27888-97.

- [84] Rother J, Büchsenschütz-Göbeler M, Nöding H, Steltenkamp S, Samwer K, Janshoff A. Cytoskeleton remodelling of confluent epithelial cells cultured on porous substrates. *Journal of The Royal Society Interface* 2015;12.
- [85] Murphy CM, Haugh MG, O'Brien FJ. The effect of mean pore size on cell attachment, proliferation and migration in collagen–glycosaminoglycan scaffolds for bone tissue engineering. *Biomaterials* 2010;31:461-6.
- [86] Jones JR, Tsigkou O, Coates EE, Stevens MM, Polak JM, Hench LL. Extracellular matrix formation and mineralization on a phosphate-free porous bioactive glass scaffold using primary human osteoblast (HOB) cells. *Biomaterials* 2007;28:1653-63.
- [87] <https://www.desktopmetal.com/>.
- [88] <https://www.8hp.com/us/en/printers/3d-printers/metals.html>.

Earlier Version